# General Disclaimer

One or more of the Following Statements may affect this Document

- This document has been reproduced from the best copy furnished by the organizational source. It is being released in the interest of making available as much information as possible.

- This document may contain data, which exceeds the sheet parameters. It was furnished in this condition by the organizational source and is the best copy available.

- This document may contain tone-on-tone or color graphs, charts and/or pictures, which have been reproduced in black and white.

- This document is paginated as submitted by the original source.

- Portions of this document are not fully legible due to the historical nature of some of the material. However, it is the best reproduction available from the original submission.

NASA CR-
147442
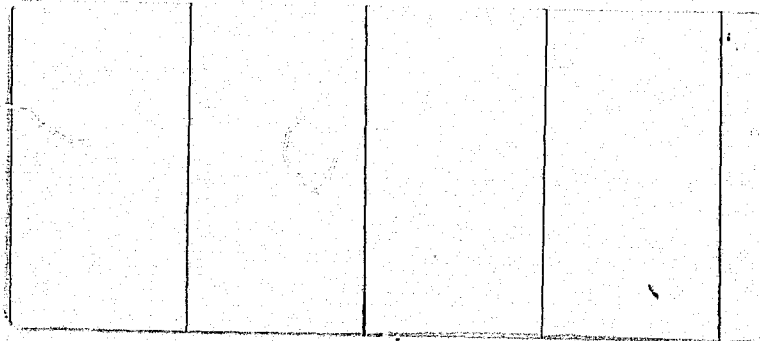
E7.6 - 1 0.1 9.0.
CR- 147442

(E76-10190)   ANALYSIS OF MICROWAVE
RADIOMETRIC MEASUREMENTS FROM SKYLAB (Naval
Research Lab.)   102 p HC $5.50   CSCL 05B

N76-18617

Unclas
G3/43   00190

NAVAL
RESEARCH
LABORATORY

WASHINGTON, D.C.

ANALYSIS OF MICROWAVE
RADIOMETRIC MEASUREMENTS FROM SKYLAB

Robert M. Lerner and James P. Hollinger

Naval Research Laboratory

Washington, D. C.   20375

Submitted to

NASA-Johnson Space Center

Houston, Texas 77058

December 1975

TABLE OF CONTENTS

ANALYSIS OF MICROWAVE

RADIOMETRIC MEASUREMENTS FROM SKYLAB

Robert M. Lerner and James P. Hollinger

Naval Research Laboratory

Washington, D. C. 20375

INTRODUCTION:

The earth-orbiting satellite SKYLAB was operated during the summer, fall and winter of 1973-74. Its orbit criss-crossed the earth at an altitude of approximately 235 nautical miles between latitudes 50N and 50S. A group of five remote earth sensing instruments was designated the Earth Resources Experimental Package (EREP). The results from two of these, S-193 and S-194, are the subject of this microwave sensor report. Their locations on SKYLAB are shown in Figure 1. The S-193 microwave sensor consisted of a scatterometer, altimeter and passive radiometer, all sharing a common parabolic dish antenna and operating at a frequency of 13.9 GHz. The antenna can be tilted 48° off-nadir in either direction along the spacecraft ground track or across this track. The S-194 radiometer employs a fixed, one meter phased array antenna with its field of view centered on nadir. The operating frequency of the S-194 is 1.4 GHz.

The objective of the investigation reported here is to establish the degree to which quantitative measurements of sea surface conditions and related wind fields can be made
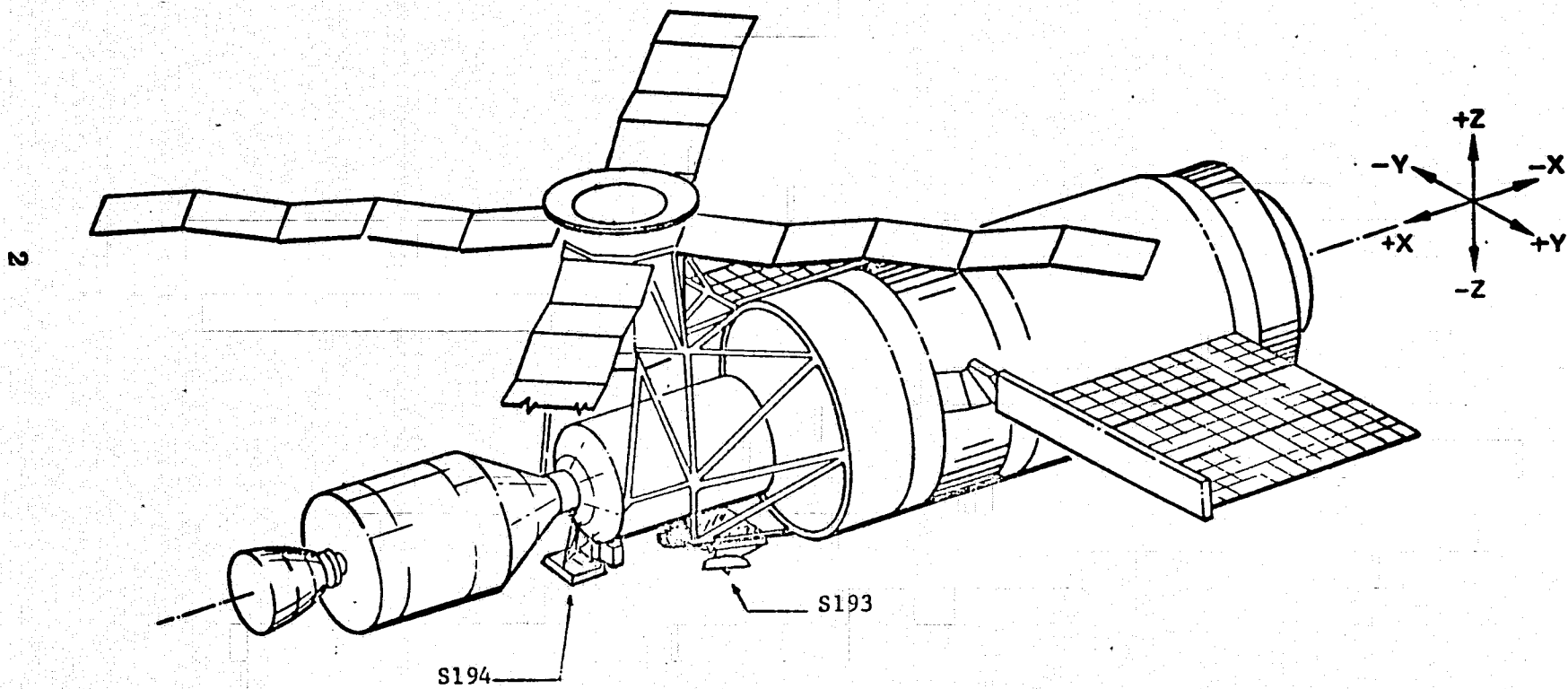
Figure 1

using the S-193 and S-194 radiometers. The first priority of the investigation is to demonstrate the reliable operation of the radiometers and the feasibility of satellite-based observations under ideal ocean and atmospheric conditions. The second priority is to examine the effects of marine wind speed, sea surface roughness and foam coverage on radiometer antenna temperature in order to evaluate the potential for passive microwave determination of ocean surface wind fields from a satellite. The third priority is to examine the effects of changes in sea salinity of selected target areas in order to test the capability of S-194 to determine sea salinity. The fourth priority is to examine the effects of a wide variety of cloud and precipitation conditions over the ocean in order to investigate the effects of these atmospheric conditions on passive microwave measurements from a satellite.

The microwave radiometer measures the absolute level of the total power received by its antenna over a particular frequency interval Δf. Although the received power may contain spurious manmade radiations at times, we are concerned only with the absolute measurement of the self radiation of the various materials composing the earth's environment. The signal received by an earth viewing radiometer is composed of not only the radiation emitted by the earth's surface, but also the downwelling sky radiation reflected from the surface, as well as the emission and attenuation of the atmosphere between the surface and the radiometer. In

general, high gain antennas receive power primarily over a relatively narrow beam or solid angle, however some power is usually received from all directions. The power received in these side lobes and back lobes, though possibly small, must be taken into account if the intensity and spatial distribution of the incident signal is to be accurately inferred from the measured total power.

In general the measured intensity distribtion is the true intensity distribution convolved with the antenna reception pattern. There are two approaches to the interpretation of the radiometric measurements. One is to obtain the true brightness distribution from the measured distribution using a detailed knowledge of the antenna pattern and any one of a number of inversion techniques (e.g. 1). It should be noted that the restoration process can only provide an intensity distribution which satisfies the convolution equation and the measurements but which is not unique since an infinite number of solutions can be found for any finite antenna pattern and set of measurements. Generally, the simplest solution consistent with the measurements is selected, or a priori knowledge of the intensity distribution is used to obtain an acceptable solution. An alternate approach, and the one adopted for this investigation, is to model the earth environment, calculate an intensity distribution, convolve it with the known antenna pattern, and compare the calculated received power with the actual measurements. The model is adjusted until the calculations agree with the

4

measurements to within the measurement error. Both approaches are equally valid and general. The latter approach may be preferred if the measurements are made only at a few restricted positions. Since, in the case of S-194 measurements are made only at nadir, the inversion technique is not practical and the latter approach was selected for all of the studies reported here.

The approach is to calculate the microwave intensity using theoretical models for the atmospheric radiation and attenuation, and for the ocean surface emission and reflection; and then to convolve this total radiation with the detailed antenna pattern. These calculations are then compared with the measurements. In order to perform the convolution, it is necessary to keep track of the polarization and intensity of the various radiations from the environment and properly reference them to the polarization and gain of the antenna. This is conveniently done by using Stokes parameters (e.g. 2) and translating from the earth oriented coordinate system, with respect to which the environmental calculations are made, to a satellite-borne antenna coordinate system. These calculations will be described in detail and then applied to measurements of increasingly complex environmental conditions as follows:

1.   Use the model and antenna pattern to correctly calculate recorded antenna temperature over ideal ocean conditions. temperature over ideal ocean conditions.

2.   Make beam corrections in the vicinity of rapidly changing signal such as land-water and water-land interfaces.

3. Measure the effect of changes in the salinity of the target area.

4. Examine the effects of changing thermodynamic water temperature.

5. Examine the effects of sea surface roughness and foam coverage.

The analysis of this report will be confined to measurements from S-194. Unfortunately, the detailed, accurate antenna pattern necessary for the analysis of S-193 data was not received until the end of this investigation and after funding had been expended. However, the complete environmental model and formalism necessary for the analysis of S-193 data hs been completed and is included in this report. It is hoped that analysis of the S-193 data can be accomplished at some future date using alternate funding.

SENSOR DESCRIPTION:

The S-193, 13.9 GHz radiometer shared a 48-inch diameter parabolic antenna with an active microwave altimeter and scatterometer. It was capable of receiving both horizontally and vertically polarized radiation. The half-power beamwidth of the S-193 was approximately 1.6°, equivalent to a nadir-looking, half-power footprint of approximately 6 nautical miles assuming a satellite altitude of 235 n.mi. The antenna is mounted in such a fashion as to make possible off-nadir scans up to 48° corresponding to 50.3° with respect to local vertical at the earth's surface.

The available scan modes were in-track contiguous (ITC), cross-tract contiguous (CTC), in-track non-contiguous (ITNC), cross-track non-contiguous right (CTNC-R), cross-track non-contiguous left (CTNC-L), and cross-track non-contiguous left and right (CTNC-L/R). The S-193 Sensor Performance Evaluation Group (S-193 SPEG) (3) determined that the standard deviation for measurements using the S-193 (radiometric precision) had an average value of 1.62°K. Dynamic range of the radiometer receiver was determined by the S-193 SPEG as being 4 to 353°K with a linearity within 4.3°K of best straight line over 350°K. The footprints for S-193 in the ITNC and CTNC-R modes are shown in Figure 2.

The S-194 operates at a center frequency of 1.414 GHz with a bandwidth of 27 MHz. It utilizes a square, planar, 8 x 8 element phased array antenna measuring one meter on a side. The half-power beamwidth was 15° with greater than 97% main-beam efficiency. This results in a half-power footprint of approximately 60 n.mi. The S-194 footprint is represented by the large circle in Figure 2. A.I.L. provided us with very complete antenna patterns taken before launch of the flight version of the S-194 antenna. The patterns consist of 72 cuts through the main-beam axis spaced every 5 degrees in azimuth. The normalized S-194 antenna response pattern, integrated over 360° in azimuth, as a function of the angle off the main-beam axis, theta, is presented in Figure 3. Also given is the percentage effective solid
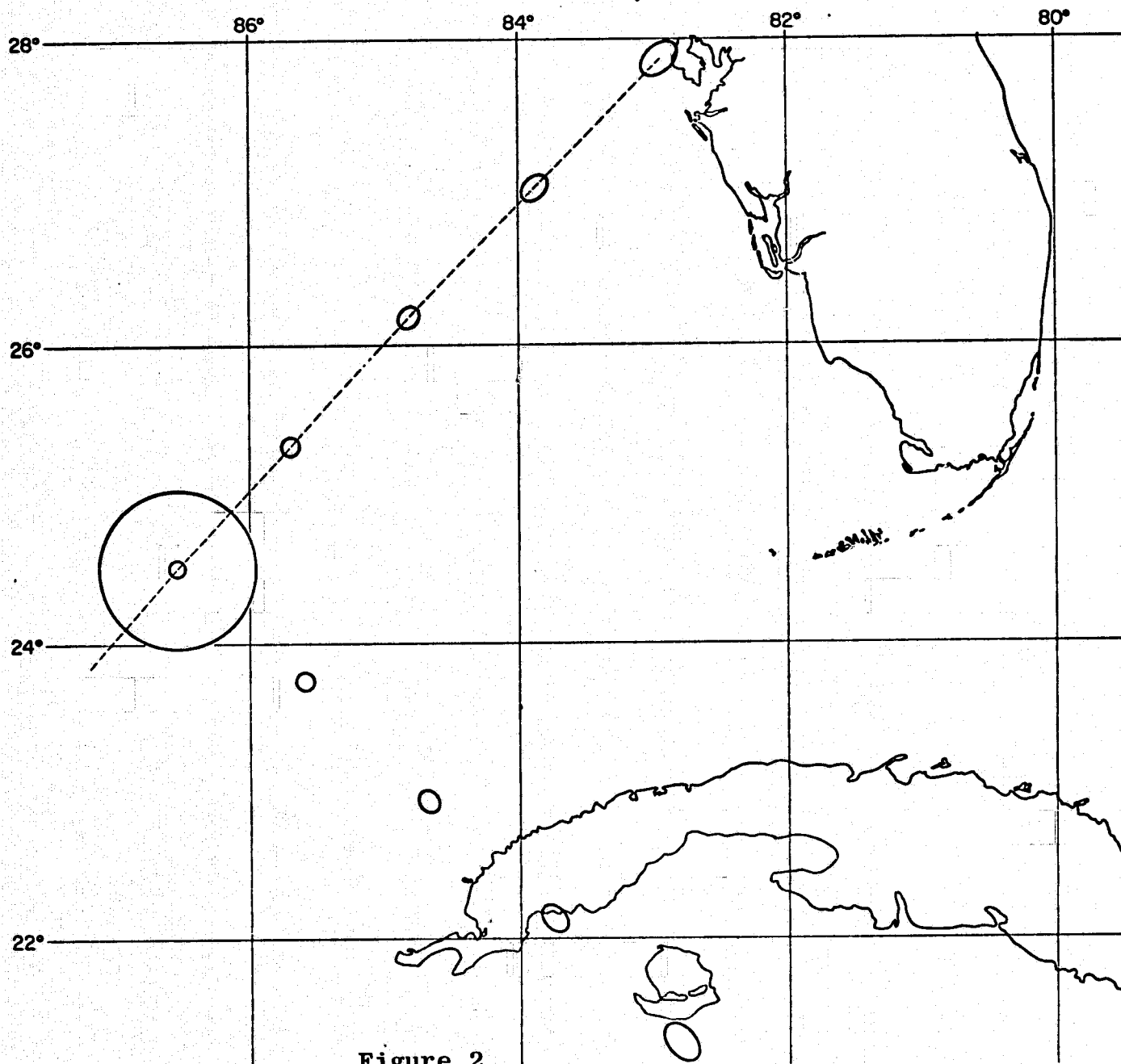
7

Figure 2

angle contained within theta as a function of theta. Although the pattern averaged in azimuth is given in Figure 3, all of the detailed pattern cuts were used in the analysis of S-194 data. The radiometer utilizes a calibration scheme referenced to a fixed "hot" and "cold" load input. The data are pulse-code modulated and recorded on magnetic tape. The "hot" and "cold" reference noise generators provide inflight calibration of the radiometer electronics. The accuracy and precision of the radiometric measurements depend on the stability and accuracy of these calibration sources.

S-194 CALIBRATION:

The first deep-space calibration pass during SL-2 provided a measured antenna temperature greatly in excess of the known L-band cosmic background temperature. The S-194 Sensor Performance Evaluation Group (S-194 SPEG) (4) determined that the pre-flight electronics box calibration must be in error. As a matter of paracticality, it was assumed that all insertion loss terms remained unchanged from their prelaunch measured values, and that the total error in the deep-space calibration could be assigned to the electronics box calibration constants C_2 and C_4. This was done since all the loss terms including C_2 and C_4 are interdependent and no one term can be determined uniquely from the flight data available. The system processing algorithms were reworked using a known value for cosmic background temperature and some pre-flight hot calibration source temperatures.
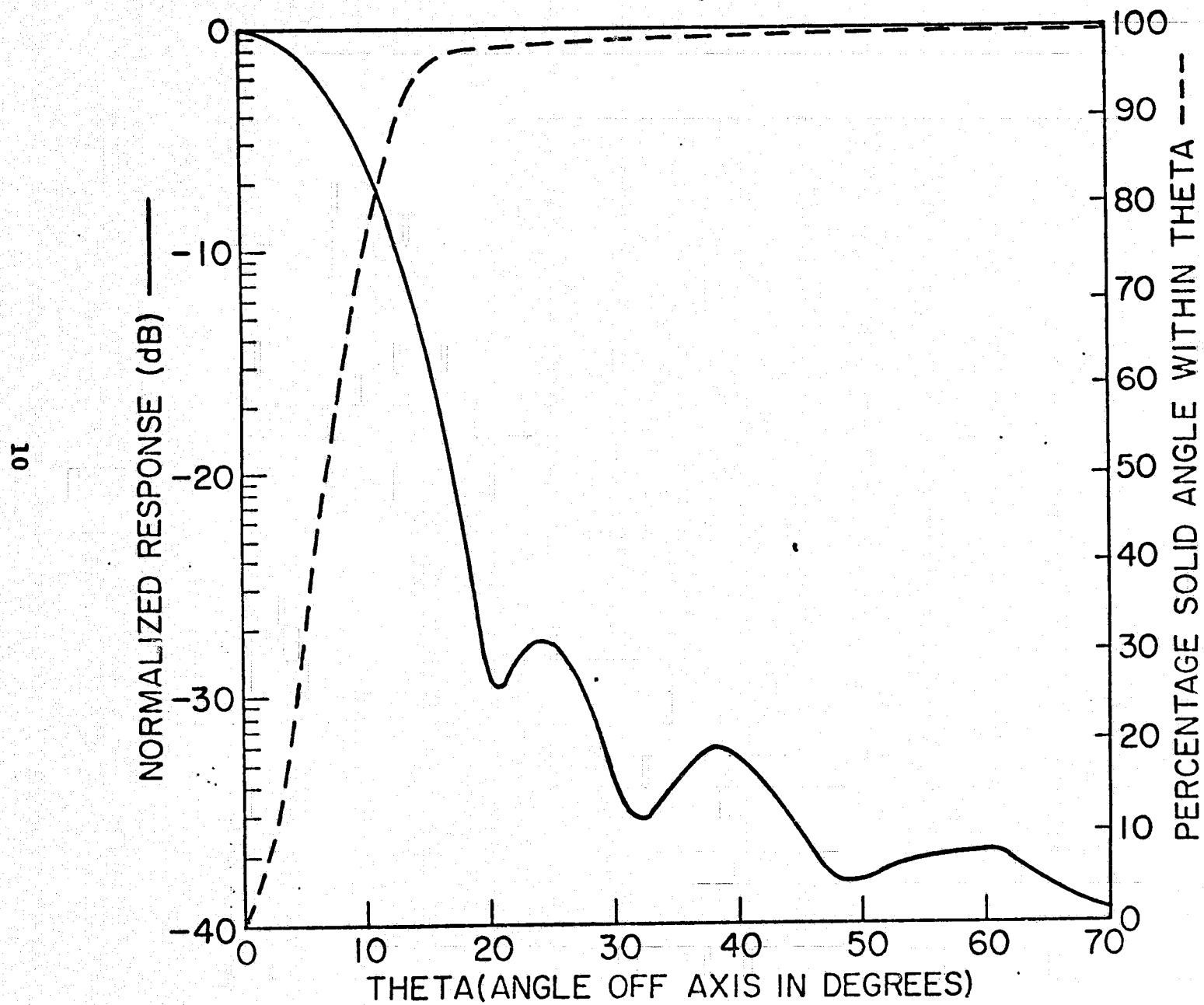
9

Figure 3

Simultaneous solutions of the reworked system equations yielded new values for C_2 and C_4. These new values were applied to the data processing for all three Skylab missions before the data was released.

As considerable amounts of data from SL-2, SL-3, and SL-4 became available, it was obvious that a second correction iteration was necessary. C_2 and C_4 were again adjusted using a slightly better value for the cosmic background temperature and a value from Pass 56 for the antenna temperature of the Gulf of Mexico. This adjustment was not included in the released data. Thus it was necessary to change each output value individually to incorporate the new values of C_2 and C_4 in the antenna temperature determination.

After reducing the available data using these values for C_2 and C_4, provided by the S-194 SPEC, and comparing with our calculations we noted a systematic offset of approximately 3.6 degrees. We then elected to further refine the system equations by using the values of 2.8°K for cosmic background temperature (18) and 95°K for the Gulf of Mexico temperature. This calculation resulted in what we now consider the best available values for C_2 and C_4. Utilizing these values provides for close agreement between all measured and calculated values. It may be argued that the adjustment in the calibration constants based upon the calculated value for the temperature of Gulf of Mexico is somewhat of a bootstrap operation and subsequent agreement between the recalibrated measurements and the calculations

11

is therefore not surprising. We feel this procedure is appropriate and analysis of the data is valid since the five measurements over the Gulf of Mexico used in the recalibration constitute a very small set of the total measurements analyzed. Further, they were taken under nearly ideal conditions of clear weather and calm seas and excellent in situ ground truth is available from ships and aircraft. Values of C_2 and C_4 were computed for each of the five Gulf of Mexico passes occurring on 6/10, 6/11, 8/8, 1/6, 1/8 1973. The average values of $C_2 = 6.2124$, $C_4 = 13.0694$ which were deduced were then used to reduce all the available data. Due to the significance of these changes in the calibration constants, we feel it is worthwhile to summarize the description of the procedure here even though it appears in S-194 SPEG report (4).

The various temperature and losses necessary for the calibration analysis are shown in Figure 4 which is similar to Figure 3.2.1.3-1 of MSC-05528. The hot reference noise generator (RNG) was an accurately known and highly stable temperature controlled device designed to provide a reliable reference for evaluating the stability of the radiometer system. In order to check the accuracy of the hot RNG, a comparison was made before Skylab flight between the true radiometric temperature of the source, and the Y-factor output from the radiometer obtained during the hot calibration mode, corrected for cable losses. The relationship between the radiometric temperature at the diode switch and

ELECTRONICS BOX

Block Diagram for Computation of Hot Cal Source Radiometric Temperature
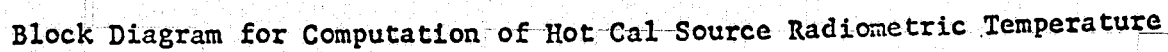
Figure 4

the computed source temperature is given by the following expressions.

$$T_{SH} = \frac{T_{PH} - (1-L_{CH})\, t_{CH}}{L_{CH}} \qquad (1)$$

$$T_{PA} = T_{SA}\, (L_{CA}) + (1-L_{CA})\, t_{CA} \qquad (2)$$

$$T_{PH} = T_{PA} \qquad (3)$$

$$T_{SH} = \frac{T_{SA}(L_{CA}) + (1-L_{CA})\, t_{CA} - (1-L_{CH})\, t_{CH}}{L_{CH}} \qquad (4)$$

where

$$t_{CH} = (T_{SH} - t_D)\, 0.157 + t_D \qquad (5)$$

$$t_{CA} = t_{CAA} + \frac{1-L_{CAB}}{1-L_{CA}}\, (t_D - t_{CAA}). \qquad (6)$$

Several basic assumptions were made in attempting to correlate the computed source temperature with the hot RNG source thermal temperature:

1. The thermal temperature of the hot RNG is its true radiometric temperature.

2. The loss factor for the cable which connects the hot RNG to the diode switch is well known.

3. The temperature of the external RF cable (T_{CAA}) is the same as the temperature of the S-194 antenna structure.

4. In the hot calibration mode $T_{PH} = T_{PA}$. The S-194 is calibrated such that for any radiometric temperature applied to the input of the RF antenna calbe would be identically recorded in the output data.

A discrepancy of 1.35°K between the computed source temperature of 371.49°K and the hot RGN thermal temperature of 372.84°K was recorded. This discrepancy was apparently due to inaccuracies in Equations (1) - (6) above.

A study of the raw data for the hot calibration periods during SL-2, SL-3, and SL-4 gave a value for the standard deviation of the radiometer output TSA of $\sigma_2 = 0.1329°K$, $\sigma_3 = 0.1538°K$, and $\sigma_4 = 0.1947°K$ over all the calibration passes for which the hot source has stabilized. There is currently no explanation for the slight increase of σ from SL-2 to SL-4.

A calibration curve relating the radiometric temperatures present at the Dicke switch and the corresponding output Y-factors can be computed from the equation*

$$\frac{A_A - A_C}{T_{PA} - T_{PC}} = \frac{A_H - A_C}{T_{PH} - T_{PC}} . \qquad (7)$$

Solving for T_{PA}

$$T_{PA} = T_{PC} + \frac{A_A - A_C}{A_H - A_C} (T_{PH} - T_{PC}) . \qquad (8)$$

---

*See reference Table 1 for definition of terms. (p.26)

The relation between the hot RNG radiometric temperature at the Dicke switch (T_{PH}) and the hot calibration radiometric temperature (T_{SH}) must include cable losses.

$$T_{PH} = T_{SH}L_{CH} + (1 - L_{CH})\, t_{CH} \tag{9}$$

This is equally true for the cold calibration radiometric temperature T_{SC}.

$$T_{PC} = T_{SC}L_{CC} + (1 - L_{CC})\, t_{CC} + (t_D - T_{SC})(1 - L_{CCB}). \tag{10}$$

Similarly,

$$T_{PA} = T_{SA}L_{CA} + (1 - L_{CA})\, t_{CA}. \tag{11}$$

There exists a relationship between the RF cable thermal temperature t_{CAA} and the orbital Beta angle (β) which is the angle between the sun vector and its projection into the orbital plane. This relationship was determined emperically for a $t_D = 297°K$ and for Beta angles between zero and 53 degrees.

$$t_{CAA} = \left[\frac{t_9 + t_{10}}{2}\right]\left[0.86 - \frac{0.38\beta}{53}\right] + \frac{101\beta}{53} + 50,$$

where

t_9 = thermal temperature values in word 9 of data frame,

16

t_{10} = thermal temperature value in word 10 of data frame.

Substituting for T_{PA}, T_{PC}, and T_{PH} in equation (8) using equations (9), (10), and (11) yields

$$T_{SA}L_{CA} + (1-L_{CA})\, t_{CA} = T_{SC}L_{CC} + (1-L_{CC})\, t_{CC} + (t_o - T_{SC})$$

$$(1-L_{CCB}) + \frac{A_A - A_C}{A_H - A_C}\left[T_{SH}L_{CH} + (1-L_{CH})\, t_{CH} \right.$$

$$\left. -T_{SC}L_{CC} - (1-L_{CC})t_{CC} - (t_o - T_{SC})(1-L_{CCB}) \right] \quad (12)$$

Solving for T_{SA},

$$T_{SA} = \frac{1}{L_{CA}}\left[T_{SC}L_{CC} + (1-L_{CC})t_{CC} - (1-L_{CA})t_{CA} + (t_D - T_{SC})(1-L_{CCB}) \right]$$

$$+ \frac{A_A - A_C}{L_{CA}\,(A_H - A_C)}\left[T_{SH}L_{CH} - T_{SC}L_{CC} + (1-L_{CH})t_{CH} \right.$$

$$\left. - (1-L_{CC})t_{CC} - (t_D - T_{SC})(1-L_{CCB}) \right] \quad .$$

Now define:

$$C_1 \equiv \frac{L_{CC}}{L_{CA}} \quad ,$$

$$C_2 \equiv \frac{1}{L_{CA}}\left[(1-L_{CC})t_{CC} - (1-L_{CA})t_{CA} + (t_D - T_{SC})(1-L_{CCB}) \right] \quad ,$$

$$C_3 \equiv \frac{L_{CH}}{L_{CA}} \quad ,$$

$$C_4 \equiv \frac{1}{L_{CA}} \left[(1-L_{CH})t_{CH} - (1-L_{CC})t_{CC} - (t_D-T_{SC})(1-L_{CCB}) \right] .$$

Hence, (Eq. 12) may now be written as

$$T_{SA} = C_1 T_{SC} + C_2 + \frac{A_A-A_C}{A_H-A_C} (C_3 T_{SH} - C_1 T_{SC} + C_4) . \tag{13}$$

Correction terms reflecting the losses in the RF cable and the changes in radiometer performance resulting from changes in operating temperature must be added to equation (13).

$$T_{SA} = C_1 T_{SC} + C_2 + \frac{A_A-A_C}{A_H-A_C} (C_3 T_{SH} - C_1 T_{SC} + C_4)$$

$$+ \frac{(1-L_{CA})(t_{CACAL}-t_{CA})}{L_{CA}} \tag{14}$$

where

$t_{CACAL} = t_W$ at the time of deep space data acquisition

$= 295°K$.

Utilizing the following values from EREP 11 lunar calibration pass, it is possible to solve for T_{SA}:

$T_{SH} = 373.0875°K, \; A_H = 15$,

$T_{SC} = 249.0179°K, \; A_C = 170,$

$t_D \;\; = 288.4948°K,$

$t_{W9} = 233.5538°K,$

$t_{W10} = 236.9276°K,$

$T_{SA} = 382.9161 - 0.8207 \, A_A .$

At orbital midnight, $A_A = 420$. Therefore at orbital midnight $T_{SA} = 38.24°K$.

The antenna corrected temperature (T_{AC}) is as follows:

$$T_{AC} = \frac{T_{SA} - (1-L_A)t_L - \left[\frac{R_A-1}{R_A+1}\right]^2 \left[t_D L_{CA} + (1-L_{CA})t_{CA} - (1-L_A)t_L\right]}{L_A\left[1 - \left[\frac{R_A-1}{R_A+1}\right]^2\right]} \qquad (15)$$

where

$$t_L = \frac{1}{6}(1.5t_{W9} + 1.5t_{W10} + t_{W5} + t_{W6} + t_{w8}) \quad .$$

See Reference Table 1 for definitions of terms.

Therefore, in terms of T_{SA},

$$t_{AC} = \frac{T_{SA}}{0.9117} - 23.40,$$

for $T_{SA} = 38.24°K$, $T_{AC} + 18.54°K$.

This is not an acceptable temperature for the cosmic background radiation which is known to be approximately 2.8°K at 1.4 GHz (18). S-194 SPEG felt that the largest part of this error was due to inaccuracies in the electronics box calibration. Re-calibration was first done using 4°K as deep space brighness temperature and data from the AIL pre-installation calibration tests for the hot source.

$$T_{SA} = C_1 T_{SC} + C_2 + \frac{A_C}{A_C - A_H}\left[C_3 T_{SH} - C_1 T_{SC} + C_4\right]$$

$$- \frac{A_A}{A_C - A_H}\left[C_3 T_{SH} - C_1 T_{SC} + C_4\right]. \tag{16}$$

Let

$$T_k = C_1 T_{SC} + C_2 , \tag{17}$$

$$K = \frac{1}{A_C - A_H}\left[C_3 T_{SH} - C_1 T_{SC} + C_4\right]. \tag{18}$$

It follows that

$$T_{SA} = (T_K + A_C K) - A_A K .$$

Now taking the hot and cold reference temperatures and the corresponding Y-factor values for these temperatures T_K, K, C_2, and C_4 may be solved for.

T_{SAH} is the external hot reference temperature and A_{AH} is the corresponding Y-factor value.

T_{SAC} is the external cold reference temperture and A_{AC} is the corresponding Y-factor value.

$$T_{SAH} = (T_K + A_C K) - A_{AH} K \tag{19}$$

$$T_{SAC} = (T_K + A_C K) - A_{AC} K \tag{20}$$

From the pre-installation test calibration

$$T_{SAH} = 372.2°K \text{ and } A_{AH} = 13.2 \text{ bit counts.}$$

20

Assuming a deep space temperature of 4°K

$$T_{AC} = \frac{T_{SA}}{0.9117} - 23.40°K = 4°K .$$

$$T_{SAC} = (23.40°K + 4°K)\ 0.9117 = 24.9806°K$$

$$A_{AC} = 420 \text{ bit counts.}$$

Solving simultaneously (19) and (20) gives

$$T_K = 238.3547°K; \quad K = 0.8536°K \text{ per bit.}$$

K is a measure of the sensitivity of the radiometer.
Applying these values to equations (17) and (18) and using
the values

$$T_{SH} = 373.0875°K,\ A_H = 15$$

$$T_{SC} = 249.0179°K,\ A_C = 170,\ C_1 = 0.9615 \text{ and } C_3 = 0.9725;$$
C_2 and C_4 are obtained.

$$C_2 = -1.0749,$$
$$C_4 = 8.9017.$$

As a result of recalibration, the correction for C_2 due to
antenna cable loss temperature becomes $(1-L_{CA}/L_{CA})\ (270.2 - t_{CA})$.
These corrected values for C_2 and C_4 derived from an assumed
deep space radiation temperature of approximately 4°K hopefully

were to result in measured antenna temperatures close to those expected from modeling and previous aircraft observation. Unfortunately examination of data from SL-2, SL-3, and SL-4 which were processed with these values of C_2 and C_4 showed discrepancies of approximately 10°K from expected values of antenna temperature.

A second adjustment to the "constants" C_2 and C_4 was then computed using data from Pass 56 over the Gulf of Mexico. This second recalibration was performed using the same general method as was used for the first recalibration try after SL-2. The major difference was that this second recalibration used only flight data rather than the combination of flight and test data used for the previous recalibration.

Using the transfer equation (15) for antenna temperature (T_{AC}), temperatures at the radiometer antenna input cable (T_{SA}) were computed from two calibration targets: Deep Space Pass LC-5 $(T_{AC} = 3.3°K)$ and the Gulf of Mexico Pass 56 $(T_{AC} = 99.0°K)$. Upon solving the equations for T_{SA}, the results were:

$T_{SA} = 23.90°K$ for Deep Space Pass LC-5

$T_{SA} = 111.12°K$ for Gulf of Mexico Pass 56.

Using these two values of T_{SA} and the equation

$$T_{SA} = C_1 T_{SC} + C_2 + \frac{(A_C - A_A)}{(A_C - A_H)} (C_3 T_{SH} - C_1 T_{SC} + C_4)$$

yields solutions for C_2 and C_4, $C_2 = 14.425$, $C_4 = 17.995$.

A new correction factor to C_2 from the cable loss temperature t_{CA} must also be used

$$\Delta C_2 = \frac{1 - L_{CA}}{L_{CA}} \; (252.5 - t_{CA}) \; .$$

To verify the accuracy of these two re-recomputed calibration constants, they were applied to six selected targets taken from SL-3. For these six targets using the existing calibration constants (i.e. C_2 and C_4 after the first recomputation which was incorporated in TR-524 outputs) the discrepancy between the measured antenna temperature and the S-194 SPEG modeled computed antenna temperature averaged approximately six percent. Using the new values for C_2 and C_4 the discrepancy is reduced to approximately seven tenths of a percent. A least square fit line for the SL-3 selected sites shows good linearity over the total dynamic range when the least values of C_2 and C_4 are used.

The computer-compatible tapes, tabulations and plots sent out to the Principal Investigators for S-194 are in error in that they are not computed using the latest values for C_2 and C_4 calculated by the S-194 SPEG . Each investigator must thus change each output value individually.

Upon utilizing these latest calibration constants in the reduction of the available data, a consistent offset of approximately 3.6°K was noted between the "corrected" data

23

and our calculations. Analysis of the method used in the recalibrations led to the substitution of a lower and more realistic radiometric antenna temperature for the Gulf of Mexico. Details of the target model used by the S-194 SPEG are not presented in MSC-05528. Our model, using data from Ho et al. (6) that may not have been available to the S-194 SPEG, provides an antenna temperature of 95°K for the Gulf of Mexico. This value is four degrees less than the 99°K used by the S-194 SPEG.

In order to calculate a correction algorithm for the corrected antenna temperature (T_{AC}), it is necessary to combine equations (14) and (15). Correct T_{SA}, T_{AC}, C_2, and C_4 are defined as T'_{SA}, T'_{AC}, C'_2, C'_4.

$$T'_{AC} = T_{AC} + \frac{(T'_{SA} - T_{SA})}{L_A \left(1 - \left[\dfrac{R_A - 1}{R_A + 1}\right]^2\right)}$$

$$\frac{T'_{SA} - T_{SA}}{L_A \left(1 - \left[\dfrac{R_A - 1}{R_A + 1}\right]^2\right)} = \frac{(C'_2 - C_2) + \dfrac{A_C - A_A}{A_C - A_H}(C'_4 - C_4)}{L_A \left(1 - \left[\dfrac{R_A - 1}{R_A + 1}\right]^2\right)}.$$

Substituting the following values:

$C_1 = 0.9615$

$C'_2 = 6.2124$

24

$$C_2 = -1.0749$$

$$C_3 = 0.9725$$

$$C_4' = 13.0694$$

$$C_4 = 8.9017$$

$$L_A = 0.9231$$

$$R_A = 1.25$$

yields

$$T_{AC}' = T_{AC} + \frac{7.2873 + \left(\frac{A_C - A_A}{A_C - A_H}\right) 4.1677}{0.9117}$$

$$T_{AC}' = T_{AC} + 7.9931 + 4.5714 \left(\frac{A_C - A_A}{A_C - A_H}\right) \tag{21}$$

where A_A, A_C, and A_H are defined in Table 1.

It is necessary for each investigator to apply equation (21) to the currently available output in order to obtain the best estimate for measured antenna temperature.

Using equation (21) to reduce the data resulted in excellent agreement with our calculations over a great variety of conditions. The difference distribution of measured values minus calculated values for eighty-six different ocean areas has a mean of $-0.0035°K$ and a standard deviation of $1.3°K$.

TABLE 1

SYMBOL	DEFINITION	VALUE
C_1 C_3	Electronics Box Calibration Constants, Evaluated from Cable Loss Data	0.9615 0.9725
C_2 C_4	Electronics Box Calibration Constants, Evaluated from System Measurements	-1.0749* 8.9017*
L_{CA}	Loss Factor of Cables Connecting Antenna Terminal to Diode Switch	0.97
L_{CAB}	Loss Factor of Portion of Antenna RF Cable within Electronics Box	0.99
L_A	Loss Factor of Antenna	0.9231
R_A	VSWR of Antenna at its Output Terminal	1.25
t_{CA}	Average Temperature of Cable Connecting Antenna Terminal to Diode Switch	
t_{CAA}	Temperature of External Portion of Cable Connecting to Antenna Terminal	
t_D	Electronics Box Enclosure Temperature	
t_{CH}	Average Temperature of Cable Connecting Hot RNG Source to Diode Switch	
t_L	Effective Loss Temperature of the Antenna	
t_{W5}, t_{W6}, t_{W8}, t_{W9}, t_{W10}	Five Antenna Thermal Temperature Monitors	
L_{CH}	Loss Factor of Cable Connecting Hot RNG Source to Diode Switch	
T_{PA}	Antenna Terminal Radiometric Temperature Referenced to the Diode Switch	
T_{PH}	Hot RNG Radiometric Temperature Referenced to Diode Switch	
T_{SH}	Hot RNG Source Temperature	
T_{PC}	Cold RNG Radiometric Temperature Referenced to the Diode Switch	
T_{SC}	Cold RNG Source Temperature	

TABLE 1 (continued)

SYMBOL	DEFINITION	VALUE
T_{SA}	Antenna Terminal Radiometric Temperature Referenced to the Input of the RF Antenna Cable	
T_{AC}	Corrected Antenna Radiometric Temperature	
A_A	Antenna Radiometric Measurement (Y-Factor Bit Count in Mode 1)	
A_H	Hot Calibration Radiometric Measurement (Y-Factor Bit Count in Mode 2)	
A_C	Cold Calibration Radiometric Measurement (Y-Factor Bit Count in Mode 3)	
L_{CC}	Loss Factor of Cable from Cold Source to Cold Source Box Terminal	
L_{CCB}	Loss Factor of Cable from Cold Source Box Terminal to Diode Switch	
t_{CC}	Thermal Temperature of Cable from Cold Source to Cold Source Box Terminal	

* These values are used in the TR-524 outputs. The values which are now considered to be more correct are
$C_2 = 6.2124$
$C_4^2 = 13.0694$

DESCRIPTION OF CALCULATIONS:

A computer program ANTTEMP was written to perform the calculations necessary to model the total brightness distribution seen by the antenna and convolve this brightness distribution with the antenna pattern in order to evaluate Skylab antenna temperature measurements. The calculations necessary to model the brightness temperature are as follows: (1) the radiation emitted by the sea, (2) the upwelling radiation emitted by the atmosphere, (3) the downwelling radiation emitted by the atmosphere and extraterrestrial sources and reflected upward from the sea surface, (4) the attenuation of the radiation emitted and reflected from the sea surface by the intervening atmosphere, (5) the transformation of the antenna properties and orientation from the satellite position and reference frame to the coordinate frame on the sea surface with respect to which (1), (2), (3), and (4) are most easily calculated, and (6) the convolution of the antenna reception pattern with the total radiation at each position over the earth's surface. Each of these calculations will be described in turn.

In order to calculate the emission and reflection of microwave radiation by the sea surface, the dielectric constant of sea water must be known. This is calculated by a subroutine DIELCON which requires the inputs of sea temperature and salinity and the observational frequency. The complex dielectric constant of water ε may be written as,

$$\varepsilon = \varepsilon_o \, (\varepsilon' - j\varepsilon'')$$

where ε_o is the dielectric constant of a vacuum. The real and imaginary parts of the relative dielectric constant of water, ε' and ε'', are well represented by

$$\varepsilon' = \frac{(\varepsilon_s - \varepsilon_\infty)}{1 + (2\pi f \tau)^2} + \varepsilon_\infty$$

and

$$\varepsilon'' = \frac{(\varepsilon_s - \varepsilon_\infty)\,(2\pi f \tau)}{1 + (2\pi f \tau)^2} + \frac{2\sigma}{f} \tag{22}$$

where f is the frequency in hertz, τ is the relaxation time in seconds, σ is the ionic conductivity in ESU (1 ESU $= 4\pi\varepsilon_o$ MHOS/meter in MKS units), ε_s is the static relative dielectric constant and ε_∞ is the relative dielectric constant at very high frequencies. Both ε_s and ε_∞ are dimensionless. The constant value of 4.9 given by Saxton and Lane (5) is used for ε_∞.

The static dielectric constant, relaxation time, and conductivity are functions of salinity and temperature. To calculate the dielectric properties of water for any combination of salinity and temperature, a second order polynomial in salinity and temperature was fitted by the method of least squares to the experimentally determined values of ε_s, τ, and σ given by Saxton and Lane (5).

This determination of the dielectric properties of water as a function of salinity and temperature is probably good to better than one percent at the frequencies of S-193 and S-194. However even greater accuracy is possible at 1.43 GHz tanks to the recent accurate measurements of Ho, Love, and Van Melle(6). Their measured values are accurate to better than 0.2 percent in ε' and 0.4 percent in ε''. Therefore the above determination is used for analysis of S-193 data but for the analysis of S-194 data we use the results of Ho et al. They give the dielectric properties of sea water at 1.43 GHz as

$$\varepsilon'(x,T) = (\varepsilon'_W + a_o + a_1 x - 1)/(a_0 + a_1 x)$$

$$\varepsilon''(x,T = (C_0 + C_1 X)(\varepsilon'_W - 1)/(a_0 + a_1 x) \qquad (23)$$

where ε'_W is the real part of the dielectric constant for distilled water at sea temperature T in degrees Celsuis; X is the chlorinity in PPP which is related to the salinity S by X = (S - 0.03)/1.805; a_0, a_1, C_0, and C_1 are coefficients; and

$$\varepsilon'_W = 85.98 - 0.271\ T - 3.70 \times 10^{-3} T^2 + 6.0 \times 10^{-5} T^3$$

$$\varepsilon''_W = 13.03 - 0.5062\ T + 9.91 \times 10^{-3} T^2 - 7.3 \times 10^{-5} T^3$$

$$a_0 = 1.0022$$

$$a_1 = 0.005786 - 1.96 \times 10^{-5}T$$

$$C_0 = 0.1564 - 4.12 \times 10^{-3}T + 2.07 \times 10^{-5}T^2 + 5.13 \times 10^{-7}T^3$$

$$C_1 = 0.02231 + 1.105 \times 10^{-3}T - 9.63 \times 10^{-6}T^2 + 4.18 \times 10^{-7}T^3.$$

Using the results of subroutine DIELCON and the angle of incidence on the sea surface θ, the Fresnel reflection coefficients for a specular air-water interface are given by

$$R_h^2 = \frac{(\cos\theta - P)^2 + Q^2}{(\cos\theta + P)^2 + Q^2} \quad ,$$

$$R_v^2 = \frac{(\varepsilon'\cos\theta - P)^2 + (\varepsilon''\cos\theta - Q)^2}{(\varepsilon'\cos\theta + P)^2 + (\varepsilon''\cos\theta + Q)^2} \quad . \tag{24}$$

The subscripts h and v refer to the horizontal and vertical linearly polarized components of the radiation defined as being when the electric field vector is perpendicular or parallel to the plane of incidence. The variables P and Q are given by:

$$P = \left\{ \frac{1}{2}\left[\sqrt{(\varepsilon' - \sin^2\theta)^2 + \varepsilon''^2} + (\varepsilon' - \sin^2\theta) \right] \right\}^{1/2}$$

and

$$Q = \left\{ \frac{1}{2}\left[\sqrt{(\varepsilon' - \sin^2\theta)^2 + \varepsilon''^2} - (\varepsilon' - \sin^2\theta) \right] \right\}^{1/2}.$$

Tabulated and plotted values of the dielectric constant and
the Fresnel reflection coefficients, using the dielectric
properties based upon the measurements of Saxton and Lane,
have been calculated from the above equations as a function
of temperature, salinity, look angle and frequency and are
available in a separate report (7). Calculations of the
brightness temperature of a specular sea, as a function of
sea salinity and sea temperature at 1.4 GHz, based upon the
dielectric properties measured by Ho, et al., are given in
Figures 5 and 6. These calculations do not include atmo-
spheric effects and are intended to display the quantitative
dependence of the brightness temperature on sea salinity and
sea temperature for S-194. Note in particular the near
independence of the brightness temperature on sea temperature
for salinities near 35 parts per thousand; typical values of
ocean salinity.

In order to sum up the various radiations and convolve
the sum with the antenna pattern, it is necessary to keep
track of the polarization and intensity of the radiations.
This is conveniently done by specifying the radiation in
terms of Stokes parameters since the Stokes parameters for
the sum of several independent radiations is the sum of the
Stokes parameters of the separate radiations. The Stokes
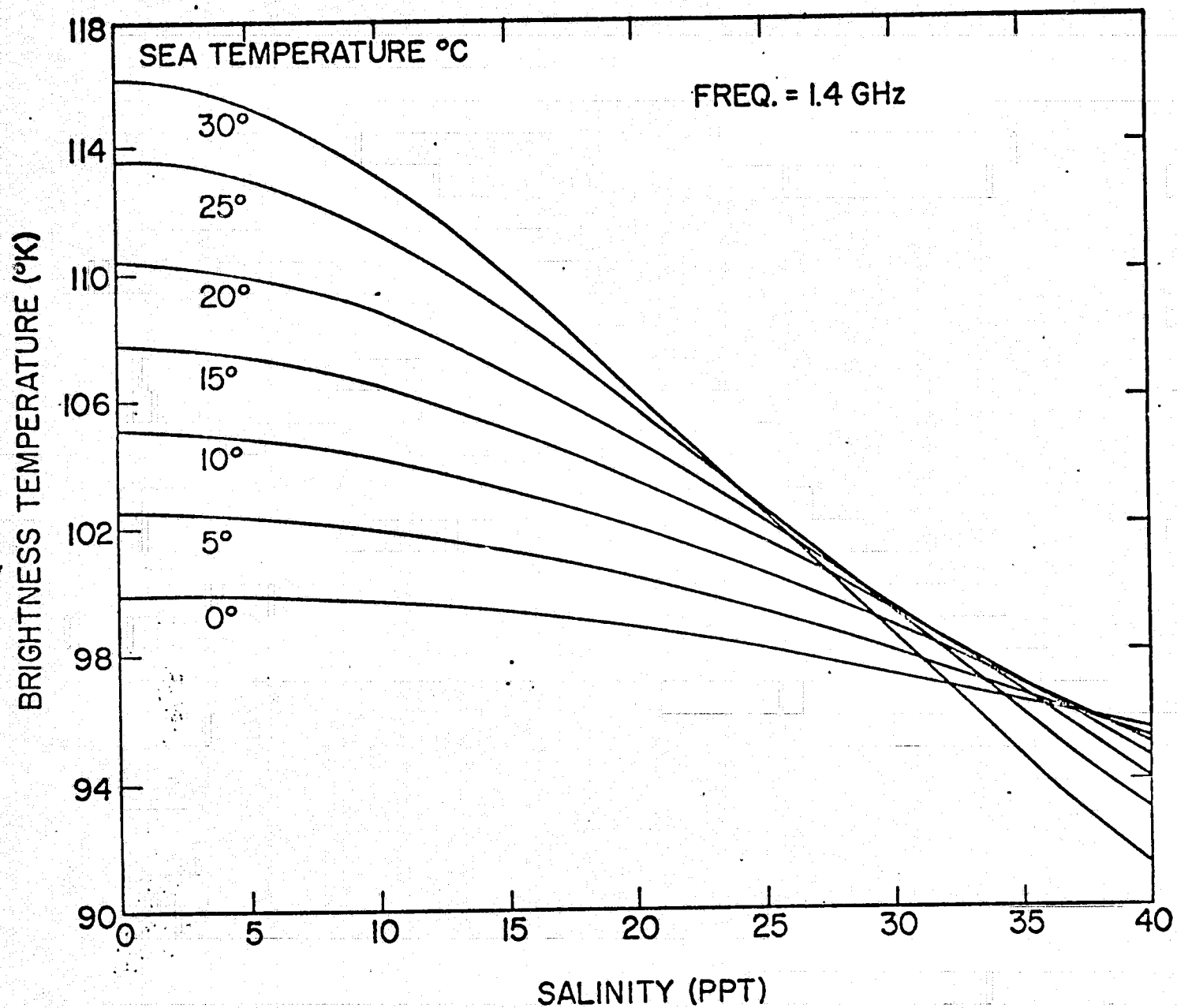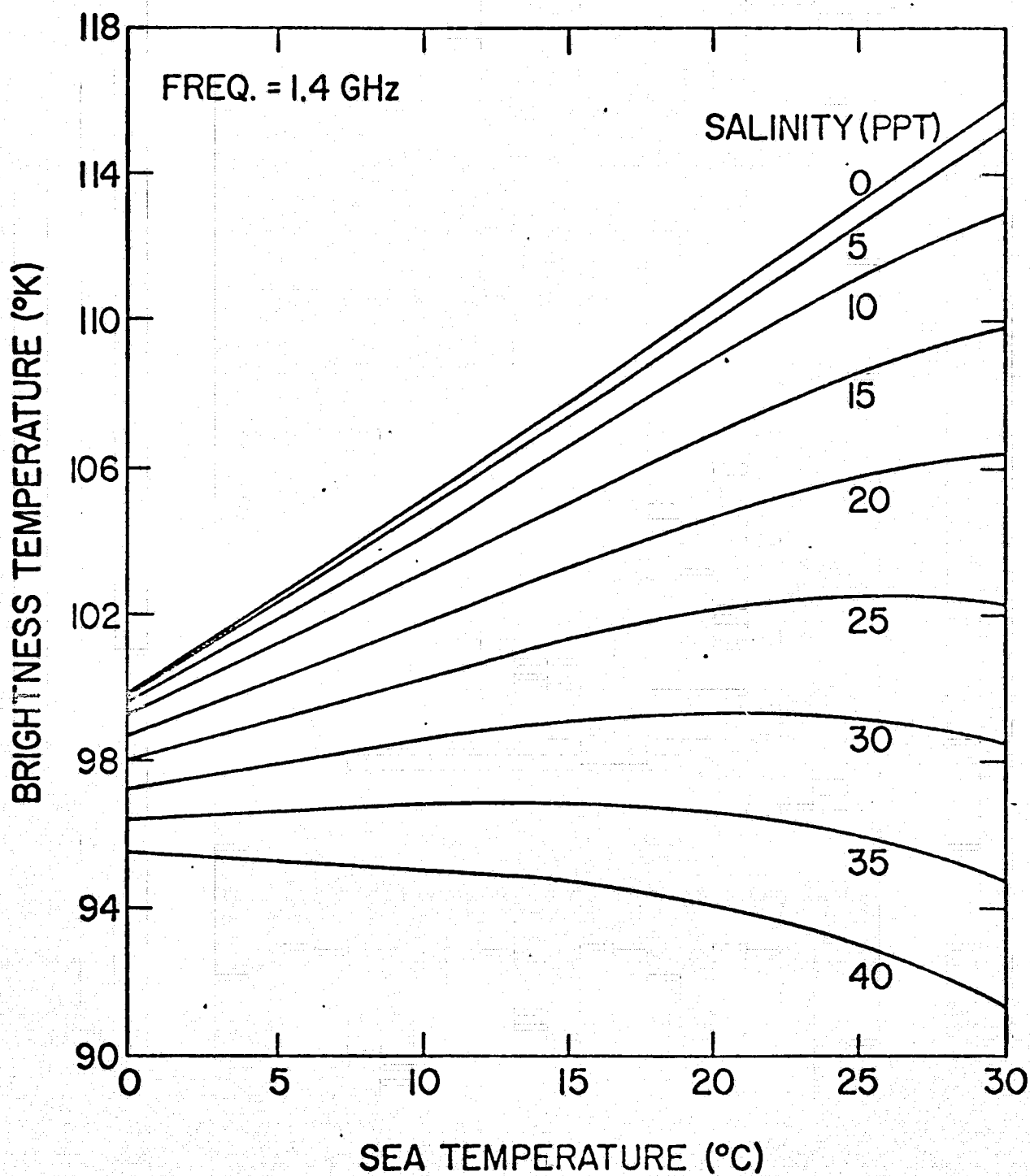parameters of the radiation emitted from a specular sea are

Figure 5

Figure 6

34

$$I_e = [1 - (R_h^2 + R_v^2)/2] \; I_{bb} \quad,$$

$$Q_e = [1 - (R_h^2 - R_v^2)/2] \; I_{bb} \quad, \tag{25}$$

$$U_e = 0,$$

$$V_e = 0 \quad.$$

where I_{bb} is the intensity of a blackbody radiator in watts/M^2/c/s/steradian and is given by

$$I_{bb} = (2hf/\lambda^2)/(e^{hf/kT} - 1) \quad. \tag{26}$$

Here h and k are Plank's and Boltzmann's constants respectively, λ is the wavelength and T the sea temperature. In most cases of microwave radiometry of the earth, and particularly at the frequencies of S-193 and S-194 the Rayleigh-Jeans approximation to Plank's blackbody radiation law is sufficiently accurate, especially when, as described later, the appropriate atmospheric boundary condition is used. We have then,

$$I_{bb} = 2kT/\lambda^2 \quad. \tag{27}$$

Note that the radiation from any source can always be described in terms of an equivalent blackbody temperature or brightness temperature. The brightness temperature T_B is the temperature to which a blackbody must be raised in order that the blackbody radiates the same intensity, at frequency

f, as does the source. This is particularly convenient when the Rayleigh-Jeans approximation is valid, for then the intensity is directly proportional to the brightness temperature.

The Stokes parameters of the downwelling atmospheric radiation, I_{sky}, reflected from the sea surface are given by

$$I_r = [(R_h^2 + R_v^2)/2] I_{sky}$$
$$Q_r = [(R_h^2 - R_v^2)/2] I_{sky} \tag{28}$$
$$U_r = 0$$
$$V_r = 0 .$$

The Stokes parameters for the emission and reflection of radiation by the sea surface given by the above equations refer to a specular sea. The effects of ocean roughness require a modification.

The microwave brightness temperature dependence on surface roughness (wind speed) arises from two effects. The first effect results from the increasing roughness of the compact water surface and the second effect from the increasing coverage of white caps and sea foam with increasing wind speed. Both effects increase with wind speed and frequency and depend upon the incidence angle and polarization. The surface roughness effect is closely coupled to the local wind field; rapidly responding to changes in the local wind

36

and hence is relatively insensitive to the energy content of low frequency gravity waves. Evidence indicates that it is primarily dependent upon the mean square surface slope and is thus due to surface waves of dimensions comparable to and shorter than the observational wavelength. The sea foam effect results from the relatively high microwave brightness temperature of sea foam and its increasing coverage with wind speed. The determination of the brightness temperature dependence on wind speed is complicated by the fact that the foam coverage of the sea surface and the roughness effect depend, not only on the local wind, but also on the air-sea temperature difference, the duration and fetch of the wind, as well as on the history of the wave spectrum of the sea area being observed.

No completely satisfactory analytical model for the microwave brightness temperature dependence on ocean roughness is available. Therefore the empirical expression

$$\Delta T_B = 0.134 \ \Delta W \ f^{1/2} \tag{29}$$

was derived from measurements. It relates the change in brightness temperature to wind speed as a function of frequency. Here ΔT_B is the increase in brightness temperature in °K, ΔW is the change in wind speed in knots and f is the observational frequency in GHz. The measurements upon which this expression is based include observations from a

bridge, an ocean tower and several different aircraft. They were made at varying incidence angles and polarizations, over a wide range in atmospheric conditions and using a variety of antenna and calibration procedures and show considerable scatter. Thus the above expression is hardly exact. But it does provide a reasonable estimate of the roughness effect at 1.41 GHz. The wind speed dependence derived from it at 1.41 GHz of 0.16°K/knot is in good agreement with measurements from an ocean tower (8) and a bridge over Cape Cod Canal (9). Since the wind speed effect changes little with incidence angle out to angles off nadir well in excess of those for which the S-194 antenna can receive significant signal, no incidence angle dependence was incorporated. The wind speed effect was taken into account in the analysis of the S-194 data by subtracting the ratio of ΔT_B divided by the sea temperature from the Fresnel reflection coefficients calculated for a specular sea.

As a first attempt to include the wind speed effect in the analysis of S-193 data, the geometric optics model as developed by Stogryn (10) was adopted. A subroutine STOGRYN was written to calculate the Stokes parameters for emission and reflection. Since no S-193 data has been analyzed, it has not been used.

The downwelling and upwelling radiation emitted by the atmosphere as well as the attenuation of radiation by the atmosphere are calculated in a subroutine ATMOS. There are

three basic parts to ATMOS, one in which the calculation of
absorption properties of significantly absorbing atmospheric
constituents as a function of density, frequency, temperature,
and pressure is done, a second part which distributes these
parameters according to an atmospheric model, and a third
which relates the resulting distribution of physical tempera-
ture and absorptivity to a radiometric temperature at any
microwave frequency.

For an atmosphere in local thermodynamic equilibrium
and wherein negligible microwave scattering occurs, the
radiometric properties may be described by an absorption
coefficient which gives the amount of energy absorbed per
unit of length along a particular direction in nepers per
kilometer. This absorption coefficient is primarily dependent
on oxygen, water vapor, and liquid water in the atmosphere
and has been expressed as a function of the densities of
these constituents and the ambient temperature and pressure
for use in ATMOS.

The absorption formulas are computed in three separate
subroutines: oxygen, water vapor, and liquid water.

Oxygen

The calculation of microwave oxygen absorption is based
on Meeks and Lilley's (11) extension of Van Vleck's (12)
work with the modification suggested by Reber (13). The
model used in ATMOS takes into account 46 fine structure

39

transitions of the O_2 molecule, 45 of them from 48 to 71 GHz and one at 118 GHz. Pressure line broadening and temperature dependence are also accounted for. The basic formula relating the absorption coefficient α in nepers per kilometer to frequency ν in gigahertz, pressure P in millimeters of mercury, and temperature T in degrees Kelvin is:

$$\alpha = \frac{CP\nu^2}{T^3} \sum_N S_N \exp\left(-\frac{E_N}{kT}\right). \tag{30}$$

Here N is the rotational quantum number which assumes only odd values from 1 to 45,

$\frac{E_N}{kT} = 2.06844 \frac{N(N+1)}{T}$ is the exponent in the Boltzman distribution factor,

$S_N = F_{N+}a_{N+} + F_{N-}a_{N-} + F_o a_{No}$ is the line strength factor

$$F_{N+} = \frac{\Delta\nu}{(\nu_{N+} - \nu)^2 + \Delta\nu^2} + \frac{\Delta\nu}{(\nu_{N+} + \nu)^2 + \Delta\nu^2},$$

$$F_{N-} = \frac{\Delta\nu}{(\nu_{N-} - \nu)^2 + \Delta\nu^2} + \frac{\Delta\nu}{(\nu_{N-} + \nu)^2 + \Delta\nu^2},$$

$$F_o = \frac{\Delta\nu}{\nu^2 + \Delta\nu^2},$$

ν_{N+} is the frequency in gigahertz of a transition from total angular momentum quantum state (including spin of the two unpaired electrons) J = N to J = N + 1,

ν_{N-} is the frequency in gigahertz of a transition from total angular momentum quantum state $J = N$ to $J = N - 1$,

$$a_{N+} = \frac{N(2N + 3)}{N + 1} \; ,$$

$$a_{N-} = \frac{(N + 1)(2N - 1)}{N} \; ,$$

$$a_{NO} = \frac{2(N^2 + N + 1)(2N + 1)}{N(N + 1)} \; ,$$

$$\Delta\nu = \left[52.7 + 0.627 (P - 20.7) \frac{300}{T} \right] \times 10^{-3} \text{ GHz or}$$

$$= \left[1.88 \, P \, \frac{300}{T} \right] \times 10^{-3} \text{ GHz whichever is less, and}$$

$$c = 0.61576.$$

Height, temperature, pressure, and frequency are inputs to the oxygen routine with the absorption coefficient as output. This analysis does not take into account high altitude Zeeman splitting (above 40 km) nor the doppler broadening above 80 km. However, since comparatively little absorption takes place due to low pressure at high altitudes, Zeeman and doppler may be neglected in almost all remote sensing applications except possibly high altitude upward looking radiometers for which a more involved computation is necessary.

Water Vapor

Microwave absorption due to water vapor is based on Staelin's (14) interpretation of Barrett and Chung's (15)

41

formula which in turn uses experimental results of several authors to extend Van Vlecks's (16) work on the subject. There is one principal rotational transition for water vapor which signigicantly affects microwaves and it has a frequency of 22.235 GHz. The equation used in ATMOS to calculate α in nepers per kilometer is:

$$\alpha = 10^5 \left\{ \frac{\nu^2 P \rho_w}{T^{3.125}} \exp\left(\frac{-644}{T}\right) \left(1+0.0147 \frac{\rho_w T}{P}\right) \left[\frac{1}{(\nu-\nu_o)^2+\Delta\nu^2} + \frac{1}{(\nu+\nu_o)^2+\Delta\nu^2} \right] \right.$$

$$\left. + 2.55 \times 10^{-8} \rho \nu^2 \frac{\Delta\nu}{T^{3/2}} \right\} \quad \text{nepers/kilometer.} \quad (31)$$

The symbols used are defined as:

ν = frequency of observation in GHz,

P = total pressure in mb,

ρ_w = water vapor density in gm/m^3,

T = temperature in °K,

ν_o = 22.235 GHz, and

$$\Delta\nu = 2.58 \times 10^{-3} \left(1 + 0.0147 \frac{\rho_w T}{P}\right) \left[\frac{P}{\frac{T}{318}}\right] 0.625.$$

Temperature, pressure, frequency and absolute humidity are inputs to the subroutine and the absorption coefficient α in nepers/ kilometer is the output.

Liquid Water

The absorption coefficient for liquid water in clouds
is based on Paris's (17) Thesis. First the real and imaginary
parts of the dielectric constant of water at a particular
temperature and frequency are computed in a separate sub-
routine which has a lower bound of -10°C, and then the
absorption coefficient is computed as:

$$\alpha = 0.0629 \left\{ \frac{3E_2}{(2 + E_1)^2 + E_2^2} \right\} \rho_L \nu. \tag{32}$$

α is in nepers per kilometer,

E_1 and E_2 are the real and imaginary parts respectively
of the dielectric constant of cloud water,

ρ_L is the density of liquid water in gm/m^3, and

ν is the observation frequency.

This approximate solution is valid for the microwave region,
and non-raining clouds wherein the drop size is much smaller
than the wavelength. (Rayleigh's limiting case of dielectric
spheres in a plane wave field.) The scattered component, it
will be noted, is negligible and what remains is the
component actually absorbed by the liquid water droplets.
Temperature, frequency, and liquid water density are inputs
to this subroutine and the absorption coefficient is the
output.

The model atmosphere used in ATMOS has a linear temperature lapse rate from the specified ground temperature to the specified tropopause height and temperature. The tropopause is taken to be at a constant temperature. An exponential pressure decay derived directly from the hydrostatic equation is set at the ground by the local barometric pressure. Oxygen is assumed to be in constant proportion and thereby specified by the pressure vs. height array. Water vapor is also exponentially modeled except for within clouds where the density is set to correspond to 100% relative humidity. Liquid water density in clouds is taken to be triangular in shape similar to clouds modeled by Paris (17). Cloud base height may be specified or optionally may be automatically determined by the point at which a parcel of air lifted adiabatically, with the potential temperature and mixing ratio constant, reaches its dew point. Cloud width and maximum density may also be specified manually or automatically by a quadratic relationship between cloud width and maximum density which was fitted to typical cumuliform cloud data so that specifying the columnar liquid water density determines the cloud size and shape.

The atmospheric radiation, I_{SKY}, is determined from the radiative transfer equation which for a non-scattering, horizontally stratified atmosphere in local thermodynamic equilibrium is given by (2),

$$\frac{dI_{SKY}}{dz} + \alpha\, I_{SKY} = \alpha\, I_{ATM}, \tag{33}$$

where α is the total absorption coefficient of the atmosphere obtained by summing the absorption coefficients due to oxygen, water vapor, and liquid water as given by equations (30), (31), and (32). I_{ATM} is the Plank blackbody function for local thermodynamic temperature T_{ATM},

$$I_{ATM} = (2h\nu^3/c^2)/(\exp[h\nu/kT_{ATM}] - 1). \tag{34}$$

The atmospheric radiation may be specified by a brightness temperature T_B defined by

$$I_{SKY} = (2h\nu^3/c^2)/(\exp[h\nu/kT_B] - 1). \tag{35}$$

The solution of equation (33) is greatly simplified when the Rayleigh-Jeans approximation to the Plank blackbody function is used since then the intensity and brightness temperature of the radiation are linearly related. Both equations (34) and (35) are then of the form

$$I = 2K\nu^2 T/c^2. \tag{36}$$

The solution of equation (33) integrated along any direction at an angle θ to the vertical and for any height h in the atmosphere is then given by

$$T_{B \text{ up}} = \int_h^\infty \alpha(z) \, T_{ATM}(z) \, L(h,z,\theta) \, dZ(\theta) + L(h,\infty,\theta) T_C \qquad (37)$$

and

$$T_{B \text{ down}} = \int_o^h \alpha(z) T_{ATM}(z) \, L(z,h,\theta) \, dZ(\theta) + L(0,h,\theta) T_g \qquad (38)$$

Here $L(a,b,\theta)$ is the transmission factor

$$L(a,b,\theta) = \exp \left\{ - \int_a^b \alpha(z) dZ(\theta) \right\} \quad , \quad \cdot \qquad (39)$$

and $dZ(\theta)$, which takes into account the earth's curvature, is given by

$$dz(\theta) = \left\{ 1 - \left[\frac{a \sin \theta}{a + h} \right]^2 \right\}^{-1/2} dz, \qquad (40)$$

where a is the earth's radius. T_C is the cosmic background temperature of 2.8°K (18) and T_g is the brightness temperature

46

of the total radiation from the ground surface. Equation (37) gives the radiometric brightness temperature of the downcoming radiation as seen looking up at an angle θ from a height h in the atmosphere. Similarly equation (38) is the upcoming radiation as seen looking down from height h. Since T_g represents the total ground radiation it is composed of both the radiation emitted by the ground and the down-welling sky radiation reflected from the ground. The downwelling sky radiation at the surface is given by equation (37) with h = 0.

The Rayleigh-Jeans approximation to Plank's law is better than one percent for frequencies less than 100 GHz and temperatures greater than 250°K. However Stogryn (19) has recently shown that the error introduced by using the Rayleigh-Jeans approximation may be reduced by at least two orders of magnitude by changing the boundary condition describing the downard flowing flux at the top of the earth's atmosphere. This improvement in accuracy is effected by replacing T_c in equation (37) by the ficticious temperature T_{cf} where,

$$T_{cf} = \frac{c^2 T}{2K\nu^2} I_c + \frac{h\nu}{2K} \, . \tag{41}$$

Here I_c is the intensity of the cosmic background radiation and is obtained from Plank's blackbody law (i.e. equation

(35) with $T_B = T_C = 2.8°K$. This change in boundary condition is also reflected in $T_{B\ down}$ as expressed by equation (38) since T_g contains the reflected downwelling sky radiation at the surface which is given by equation (37) with $h = 0$. I_{SKY} is given by (35) using T_B from (37) or (38) as appropriate.

ATMOS does a Simpson's rule integration of the above equations to obtain either T_{up} or T_{down} at angle θ from height h. The number of divisions and upper limit of the contributing atmosphere are set manually.

Figure 7 is an example of the upward looking loss due to the separate contributing atmospheric parameters, molecular oxygen, water vapor and liquid water, as generated by ATMOS. The relative effect of the three constituents can be seen from 0 to 50 GHz. The calculations are for a standard atmosphere. The integrated columnar water vapor densities (also called precipitable water) of 1.0, 3.5, and 6.0 gm/cm^2 are typical values for a dry winter day, an average day and a very humid summer day, respectively, at Washington, D. C. The liquid water columnar densities of 0.04 and 0.2 gm/cm^2 represent typical stratocumulus, the majority of clouds, and moist cumulus clouds, respectively. As can be seen atmospheric effects are most pronounced at frequencies above about 10 GHz. Therefore they are very important for the interpretation of S-193 data but relatively unimportant for the analysis of S-194 measurements. Not only are atmospheric effects small at the 1.4 GHz frequency of S-194 but there is very little

ATMOSPHRIC LOSS (PERCENT)

FREQUENCY (GHZ)

-CLOUD 0.2 GM/CM^2

WATER VAPOR

-6.0 GM/CM^2

3.5 GM/CM^2-

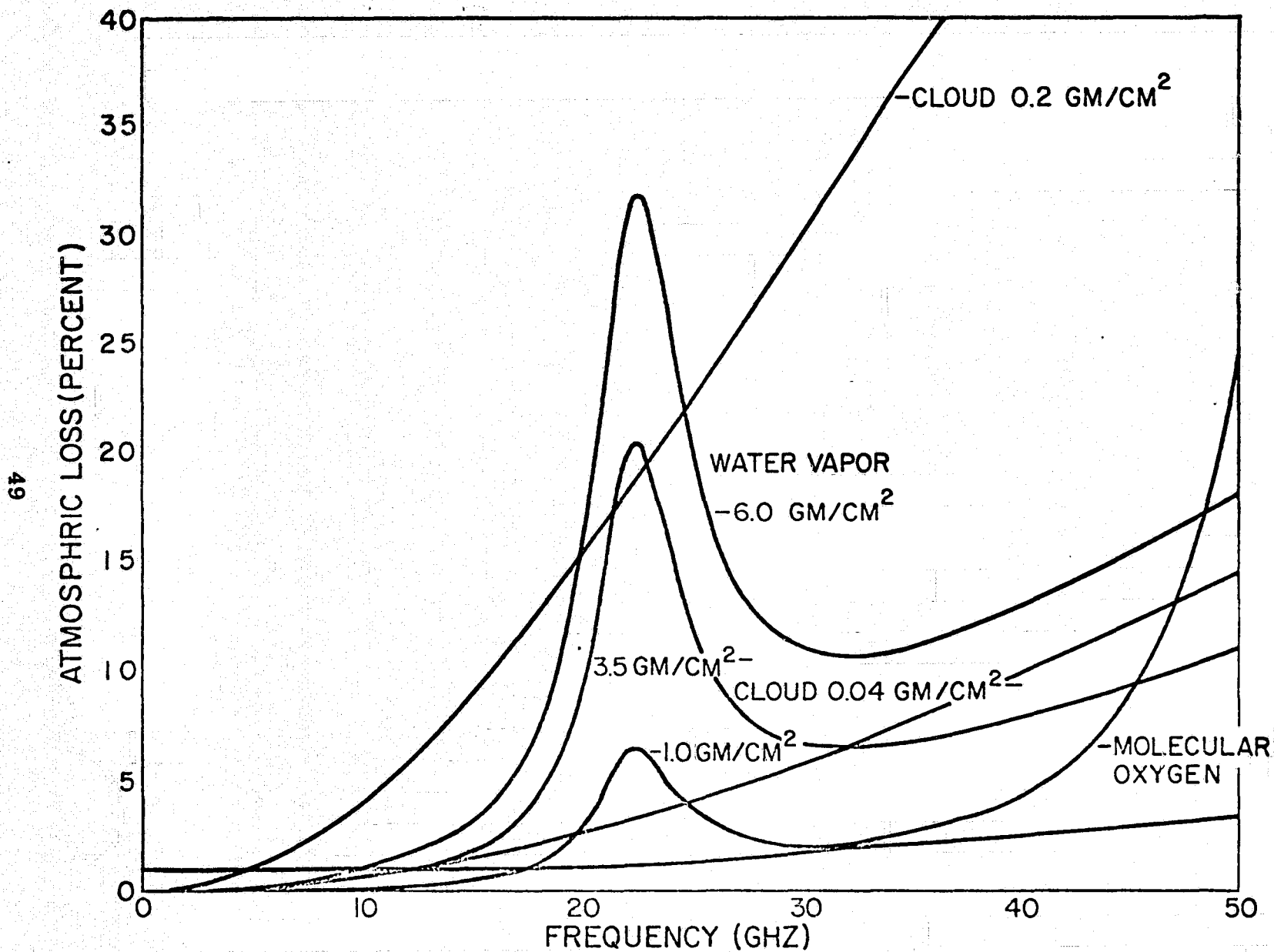CLOUD 0.04 GM/CM^2-

-1.0 GM/CM^2-

-MOLECULAR OXYGEN

Figure 7

variations from clear, dry conditions to overcast with rain. Only the most severe downpour results in any significant change at 1.4 GHz. The effective atmospheric correction for the S-194 measurements amounted to an average increase of about 5.2°K and varied only a few tenths of a degree over the entire range of the measurements.

It is necessary to translate the complete gain and polarization properties of a satellite-borne antenna from a coordinate system referenced to the antenna, with respect to which the antenna properties are most naturally and normally measured, to a coordinate system oriented with respect to the local vertical and compass points of some observed location on the earth's surface, with respect to which radiation reflected and emitted from the earth is most naturally expressed. This translation will allow the power received by the antenna from any source of specified extent, intensity and polarization to be readily calculated.

The earth-satellite geometry is shown in Figure 8. The unit vectors $(\hat{i}, \hat{j}, \hat{k})$ form an orthogonal coordinate system with the origin at the center of the earth. The earth's axis lies in the $(\hat{j}, \hat{K})$ plane with north in the direction of the unit vector $\hat{N}$. The satellite lies on the $\hat{k}$ axis at a height h above the earth's surface. It is moving in the direction of the unit vector $\hat{s}$, which is orthogonal to $\hat{k}$, at a heading H measured from north through east in the plane tangent to the earth at the sub-satellite point. The antenna is pointed in the direction of the unit vector $\hat{\mu}_o$ and views
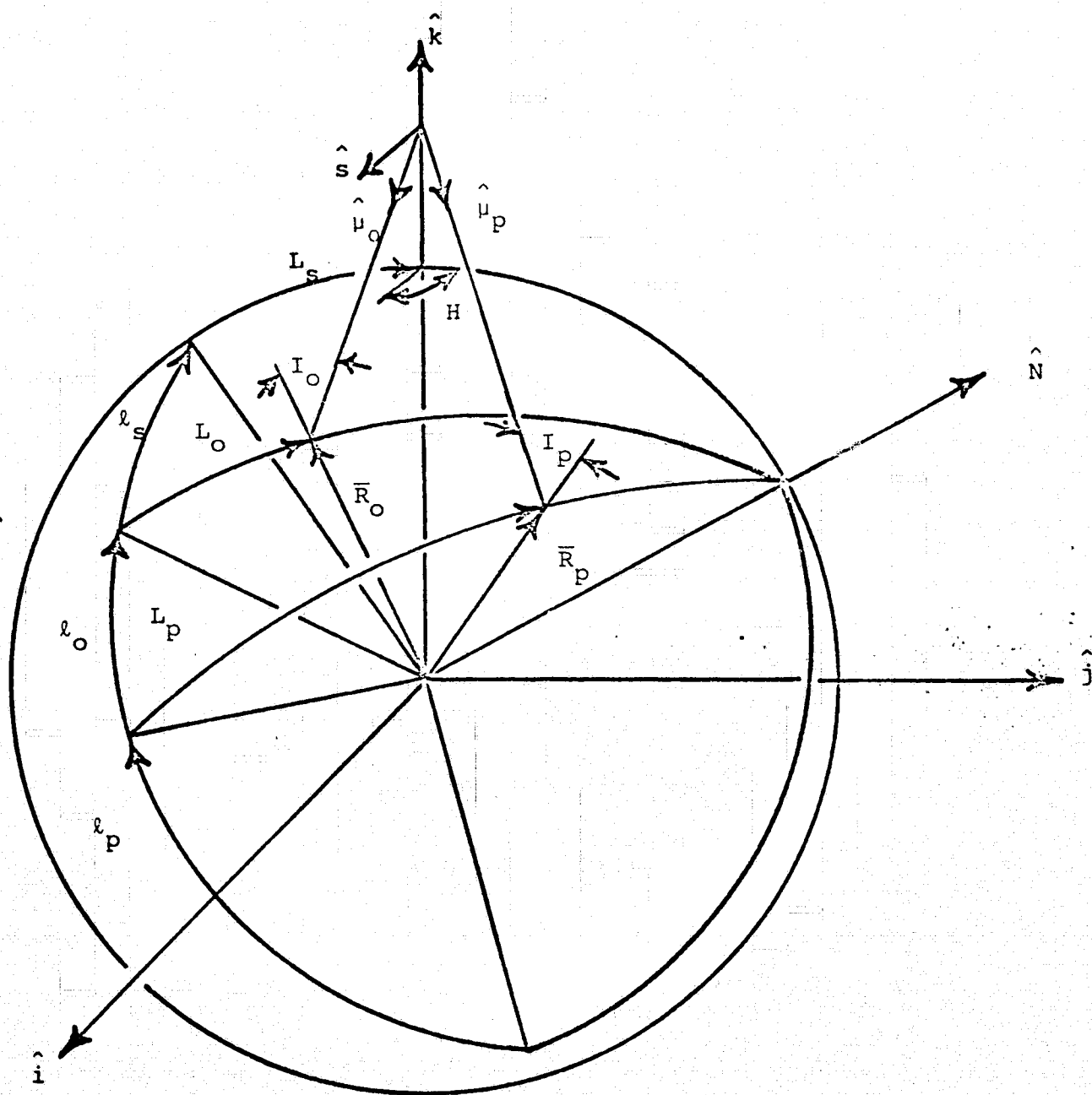
50

Figure 8

51

a point on the earth's surface located by the vector $\overline{R}_o$ from the earth's center. The angle of incidence on the earth's surface is given by I_o. The variable point for integration over the antenna beam is located at $\overline{R}_p$ in the direction $\hat{\mu}_p$ with an incidence angle on the surface of I_p. The latitude and longitude of the sub-satellite point, the antenna look point, and the integration point are given by (L_s, ℓ_s), (L_o, ℓ_o) and (L_p, ℓ_p), respectively.

The satellite is located at $\overline{R}_s$ and letting the radius of the earth be given by a, we have,

$$\overline{R}_s = (a + h)\ \hat{k}, \tag{42}$$

$$\hat{s} = \sin H\ \hat{i} + \cos H\ \hat{j}, \tag{43}$$

$$\hat{N} = \cos L_s\ \hat{j} + \sin L_s\ \hat{k}, \tag{44}$$

$$\overline{R}_o = \overline{R}_s - \{(a+h)\ \hat{\mu}_o \cdot \hat{k} + \sqrt{a^2 - (a+h)^2\ [1-(\hat{\mu}_o \cdot \hat{k})^2]}\ \}\hat{\mu}_o, \tag{45}$$

$$\cos I_o = -\ \hat{\mu}_o \cdot \overline{R}_o/a, \tag{46}$$

$$\sin L_o = \hat{N} \cdot \overline{R}_o/a, \tag{47}$$

$$\cos (\ell_s - \ell_o) = \hat{i} \cdot (\hat{N} \times \overline{R}_o/a)/\cos L_o. \tag{48}$$

Expressions for $\overline{R}_p$, I_p, L_p and ℓ_p are given by changing the subscripts o to p in equations (45), (46), (47) and (48).

The antenna properties may be conveniently specified in a spherical coordinate system referenced to the antenna and

expressed in terms of Stokes parameters as shown in Figure 9. The unit vectors $(\hat{\mu}_o, \hat{\mu}_h, \hat{\mu}_v)$ form an orthogonal coordinate system as do the unit vectors $(\hat{\mu}_p, \hat{\mu}_\theta, \hat{\mu}_\phi)$. The direction of maximum response of the antenna would generally be in the direction of $\hat{\mu}_o$ with the aperture plane coinciding with the $(\hat{\mu}_h, \hat{\mu}_v)$ plane. The Stokes parameters are given in normalized form as

$$I_a(\theta,\phi) = f(\theta,\phi)$$

$$Q_a(\theta,\phi) = f(\theta,\phi) \cos(2\beta) \cos(2\chi) \tag{49}$$

$$U_a(\theta,\phi) = f(\theta,\phi) \cos(2\beta) \sin(2\chi)$$

$$V_a(\theta,\phi) = f(\theta,\phi) \sin(2\beta) ,$$

where $f(o,o) = 1$, χ specifies the orientation of the major axis of the polarization ellipse and $\tan \beta$ is equal to the ratio of the minor axis to the major axis. A "perfect" linearly polarized antenna would have $\beta = 0$. It might be described to be "vertically" polarized when the electric vector of its radiation pattern coincides with the meridian planes of a sphere with a polar axis in the direction $\hat{\mu}_v$. In this case $\cot \chi_v = \cos \theta \tan \phi$. Naturally $I_a(\theta,\phi)$ must be zero in the direction of the poles since the meridians coverge at the poles and χ_v is not uniquely given there. A "horizontally" polarized antenna would be specified by having the electric vector of its radiation pattern orthogonal to the meridian planes; i.e. $\chi_h = \chi_v + \pi/2$.
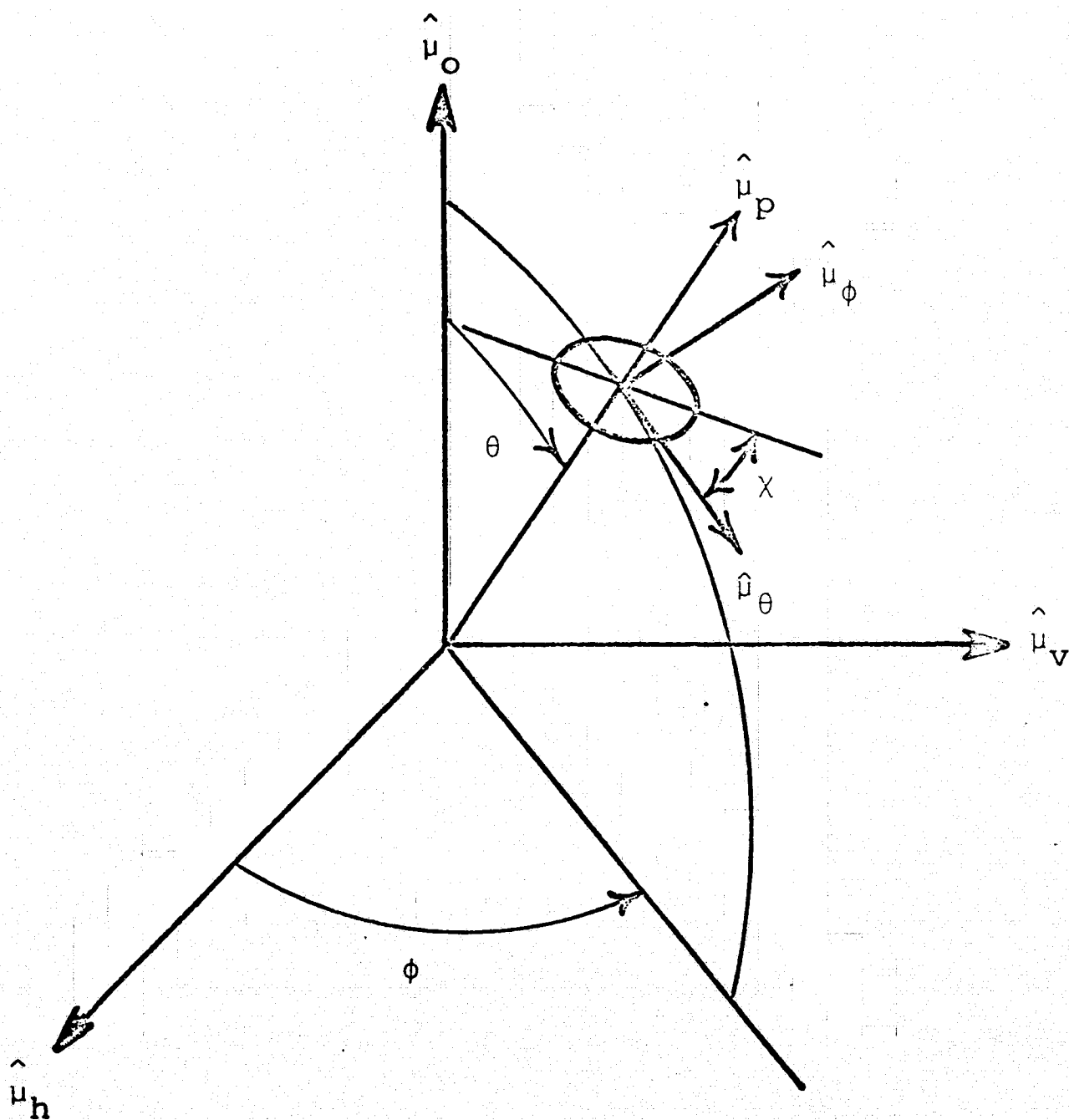
Figure 9

The Stokes parameters referenced to a second coordinate system, indicated by primes, where $\hat{\mu}_p' = \hat{\mu}_p$ but $\hat{\mu}_\theta'$ and $\hat{\mu}_\phi'$ are rotated, in the positive sense, about $\hat{\mu}_p$ by an angle $\Delta\chi$ from $\hat{\mu}_\theta$ and $\hat{\mu}_\phi$, are related to those of the unprimed system by

$$I' = I$$
$$Q' = Q \cos (2\Delta\chi) + U \sin (2\Delta\chi) \qquad (50)$$
$$U' = U \cos (2\Delta\chi) - Q \sin (2\Delta\chi)$$
$$V' = V.$$

The rotation $\Delta\chi$ necessary to reference the antenna Stokes parameters to a coordinate system where $\hat{\mu}_\theta'$ is perpendicular to, and $\hat{\mu}_\phi'$ lies in, the plane of incidence at the integration point on the earth's surface is given by

$$\cos \Delta\chi = \hat{\mu}_\theta \cdot [\bar{R}_p \times \hat{\mu}_p]/[a \sin I_p] \quad . \qquad (51)$$

The unit vectors $(\hat{\mu}_p, \hat{\mu}_\theta, \hat{\mu}_\phi)$ are given in terms of $(\hat{\mu}_o, \hat{\mu}_h, \hat{\mu}_v)$ by,

$$\hat{\mu}_p = \sin \theta \cos \phi \, \hat{\mu}_h + \sin \theta \sin \phi \, \hat{\mu}_v + \cos \theta \, \hat{\mu}_o$$
$$\hat{\mu}_\theta = \cos \theta \cos \phi \, \hat{\mu}_h + \cos \theta \sin \phi \, \hat{\mu}_v - \sin \theta \, \hat{\mu}_o \qquad (52)$$
$$\hat{\mu}_\phi = - \sin \phi \, \hat{\mu}_h + \cos \phi \, \hat{\mu}_v .$$

It is now necessary to relate the antenna coordinate system to the coordinate system fixed in the satellite. This may be done by the use of modified Euler's angles (ψ_1, ψ_2, ψ_3) as shown in Figure 10. Here the line of Nodes is given by $\hat{k} \times \hat{\mu}_o$ and

$$\hat{\mu}_{\text{п}} = [\sin \psi_2 \sin \psi_3 - \cos \psi_1 \cos \psi_2 \cos \psi_3] \hat{s}$$
$$+ [\cos \psi_2 \sin \psi_3 + \cos \psi_1 \sin \psi_2 \cos \psi_3] \hat{k} \times \hat{s} \qquad (53)$$
$$+ [- \sin \psi_1 \cos \psi_3] \hat{k}$$

$$\hat{\mu}_v = [\sin \psi_2 \cos \psi_3 + \cos \psi_1 \cos \psi_2 \sin \psi_3] \hat{s}$$
$$+ [\cos \psi_2 \cos \psi_3 - \cos \psi_1 \sin \psi_2 \sin \psi_3] \hat{k} \times \hat{s} \qquad (54)$$
$$+ \sin \psi_1 \sin \psi_3] \hat{k} \qquad .$$

$$\hat{\mu}_o = [\sin \psi_1 \cos \psi_2] \hat{s}$$
$$+ [- \sin \psi_1 \sin \psi_2] \hat{k} \times \hat{s}$$
$$+ [- \cos \psi_1] \hat{k}. \qquad (55)$$

Note that if the antenna is scannned along the in-track direction, that is $\hat{\mu}_o$ is scanned in the ($\hat{s}$, $\hat{k}$) plane,

$$\psi_1 = \psi_I = \text{INTRACK SCAN ANGLE}$$
$$\psi_2 = 0 \qquad (56)$$
$$\psi_3 = \pi/2.$$
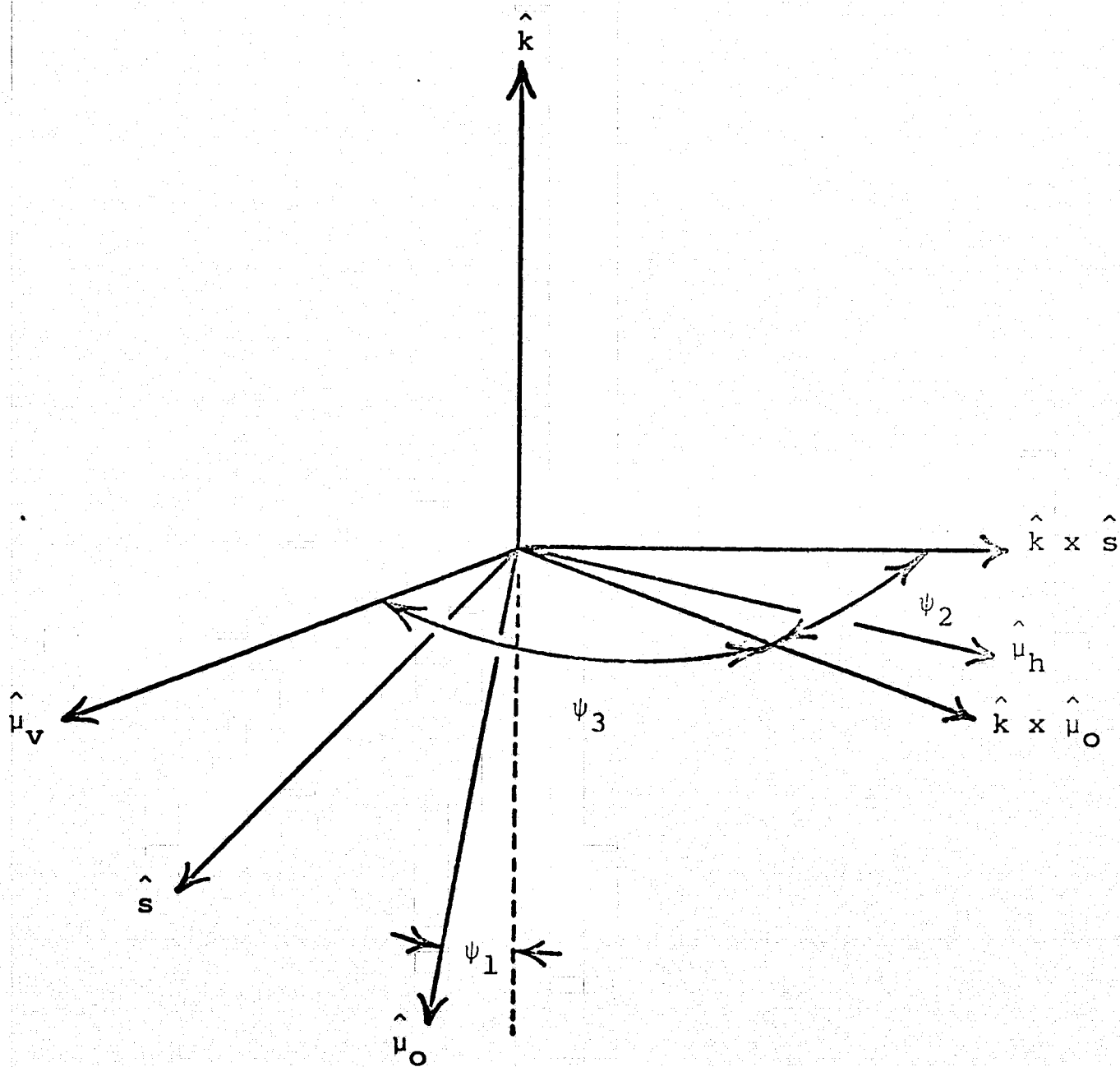
Figure 10

For cross-track scanning, where $\hat{\mu}_o$ is scanned in the $(\hat{k}, \hat{k} \times \hat{s})$ plane,

$$\psi_1 = \psi_c = \text{CROSSTRACK SCAN ANGLE}$$
$$\psi_2 = - \pi/2 \qquad\qquad\qquad (57)$$
$$\psi_3 = \pi.$$

For scanning along the surface of a cone with its axis in the $-\hat{k}$ direction,

$$\psi_1 = \text{APEX ANGLE OF CONE}$$
$$\psi_2 = \text{CONE SCAN ANGLE} \qquad\qquad (58)$$
$$\psi_3 = \pi/2.$$

Substituting (43), (53), (54), and (55) into (52) gives $\hat{\mu}_p$ in the earth centered coordinate system and expressed in terms of Euler's angles and the antenna integration angles,

$$
\begin{aligned}
\hat{\mu}_p = \;& [\cos\theta\sin\psi_1\sin(H+\psi_2) - \sin\theta\cos(H+\psi_2)\sin(\phi+\psi_3) \\
& \qquad\qquad - \sin\theta\cos\psi_1\sin(H+\psi_2)\cos(\phi+\psi_3)] \; \hat{i} \\
& + [\cos\theta\sin\psi_1\cos(H+\psi_2) + \sin\theta\sin(H+\psi_2)\sin(\phi+\psi_3) \qquad (59) \\
& \qquad\qquad - \sin\theta\cos\psi_1\cos(H+\psi_3)\cos(\phi+\psi_3)] \; \hat{j} \\
& + [- \cos\theta\cos\psi_1 - \sin\theta\sin\psi_1\cos(\phi+\psi_3)] \; \hat{k}.
\end{aligned}
$$

$\hat{\mu}_\theta$ may be obtained by replacing θ with $(\theta+\pi/2)$ in (59) and $\hat{\mu}_p$ becomes $\hat{\mu}_o$ when $\theta = 0$.

Given the orientation of the antenna with respect to the satellite ψ_1, ψ_2, and ψ_3, the satellite coordinates, altitude and heading, L_s, ℓ_s, h and H and the running variables of integration θ and ϕ, the angle of incidence and coordinates at the look point I_o, L_o, and ℓ_o and the angle of incidence and rotation angle for the Stokes parameters at the integration point I_p and $\Delta\chi$ may be found from equations (42), (44), (45), (46), (47), (48), (51) and (59) to be:

$$\sin I_o = (1 + h/a) \sin \psi_1, \qquad (60)$$

$$\sin L_o = \sin L_s \cos(I_o - \psi_1) + \cos L_s \sin(I_o - \psi_1) \cos(H + \psi_2) \qquad (61)$$

$$\cos(\ell_s - \ell_o) = [\cos L_s \cos(I_o - \psi_1)$$
$$- \sin L_s \sin(I_o - \psi_1) \cos(H + \psi_2)]/\cos L_o, \qquad (62)$$

$$\sin I_p = (1 + h/a) \sqrt{1 - [\cos\theta\cos\psi_1 + \sin\theta\sin\psi_1\cos(\phi + \psi_3)]^2} \qquad (63)$$

$$\cos \Delta\chi = (1 + h/a) \sin\psi_1 \sin(\phi + \psi_3)/\sin I_p. \qquad (64)$$

The Stokes parameters of the radiation incident on the antenna are found by summing the Stokes parameters of the radiation emitted and reflected from the sea and emitted by the atmosphere and applying the appropriate atmospheric

attenuation. Let the Stokes parameters of the total radiation be given by $[I_t, Q_t, U_t, V_t]$ and the Stokes parameters of the antenna, properly translated, be represented by $[I_a, Q_a, U_a, V_a]$, then the power received by the antenna per unit frequency interval is, e.g. (20),

$$P = (A_e/2) \int [I_t I_a + Q_t Q_a + U_t U_a + V_t V_a] \, d\Omega \, , \qquad (65)$$

where A_e is the effective area of the antenna. The effective area may be found from the normalized antenna response pattern $f(\theta, \phi)$ and a measurement of the radiation efficiency η of the antenna or a measurement of the maximum gain of the antenna G_o where

$$A_e = \eta \lambda^2 / \int f_{(\theta, \phi)} \, d\Omega = \lambda^2 G_o / 4\pi \qquad . \qquad (66)$$

Measurement of η is generally very difficult in practice and, since it is usually very close to unity, it is often taken to be one.

The power received by the antenna is often specified in terms of the so called antenna temperature T_A. This is the temperature to which an impedance, equal to the impedance of the antenna, would have to be raised in order that when it is substituted for the antenna it deliver the same power to the input of the receiver, as does the antenna. The antenna

temperature is related to the power received per unit
frequency interval by

$$T_A = P/k \quad . \tag{67}$$

Equation (65) is then the desired integration of the
total radiation incident on the antenna over the antenna
reception pattern. It represents the principal output of
ANTTEMP and is quite general.

Solar radiation reflected from the sea surface can be
appreciable; especially at 1.4 GHz. It is strongly dependent
on the ocean surface roughness. In order to calculate the
"sun glint" scattered into the antenna from the ocean surface,
the rough surface scattering or geometrics optics model as
developed by Stogryn (10) was used. Following Stogryn, and
assuming the radiation from the sun is unpolarized with a
brightness temperature T_{sun}, the brightness temperature of
the horizontally polarized radiation scattered in the direction
(θ, ϕ) is given by

$$T_h = \frac{1}{4\pi} \int T_{sun} (\gamma_{hh} + \gamma_{hv}) \, d\Omega \quad . \tag{68}$$

Since $(\gamma_{hh} + \gamma_{hv})$ changes very little over the relatively very
small solid angle subtended by the sun

$$t_h = \frac{T_{sun} \, \Omega_{sun}}{4\pi} (\gamma_{hh} + \gamma_{hv}) \quad , \tag{69}$$

61

where Ω_{sun} is the solid angle of the sun. The scattering coefficient is given by

$$\gamma_{hh} + \gamma_{hv} = \frac{(\alpha^2 + \beta^2 + B^2)}{2g^2 B^4 \cos \theta} (R_h^2 \cos^2 A + R_v^2 \sin^2 A) \, e^{- \frac{(\alpha^2 + \beta^2)}{2g^2 B^2}} \tag{70}$$

where R_h^2 and R_v^2 are the Fresnel reflection coefficients evaluated at an angle i and

$$\cos i = \frac{1}{2} (\alpha^2 + \beta^2 + B^2)^{1/2} \, ,$$

$$\alpha = \sin \theta \cos \phi + \sin \theta_{sun} \, ,$$

$$\beta = \sin \theta \sin \phi \, ,$$

$$B = \cos \theta + \cos \theta_{sun} \, ,$$

$$\sin^2 A = \frac{\sin^2 \phi \, \sin^2 \theta_{sun}}{\sin^2 (2i)} \, ,$$

$$g^2 = 0.0015 + 0.00131 \, W. \tag{71}$$

Here θ_{sun} is the incidence angle of the sun on the mean surface and W is the marine wind speed in knots. The mean-square surface slope, g^2, was obtained from Cox and Munk (21), (22) by averaging the mean-square slopes in the upwind-downwind and crosswind directions that they derived from measurements of the sun's glitter pattern on the ocean. The brightness temperature of the vertically polarized radiation, T_v, is obtained from equations (69) and (70) by interchanging the subscripts h and v throughout. The Stokes parameters for the scattered solar

radiation are given by,

$$I_s = \frac{K}{\lambda^2} (T_h + T_v) \quad ,$$

$$Q_s = \frac{K}{\lambda^2} (T_h - T_v) \quad ,$$

$$U_s = 0 \quad ,$$

$$V_s = 0 \quad . \hspace{6cm} (72)$$

Adopting one-half degree for the diameter of the solar disc and 10^5 °K for the solar brightness temperature at 1.4 GHz (20), the antenna temperature increase due to sun glint was calculated using ANTTEMP and is given in Figure 11 as a function of the solar incidence angle on the surface for several surface wind speeds. As can be seen, the effects of sun glint decrease rapidly with solar incidence angle and wind speed but can be significant. These calculations, though serving to show the qualitative dependence on solar incidence angle and wind speed, can only be regarded as approximate because of the uncertainty in the scattering coefficient. There is some evidence (8) that the effective mean-square surface slope at 1.4 GHz is only one-third of that given by equation (71). This results from surface structure smaller than about one observational wavelength, 22 cm at 1.4 GHz, being ineffective in scattering 1.4 GHz radiation. Since the short surface wavelengths contribute

Figure 11

64
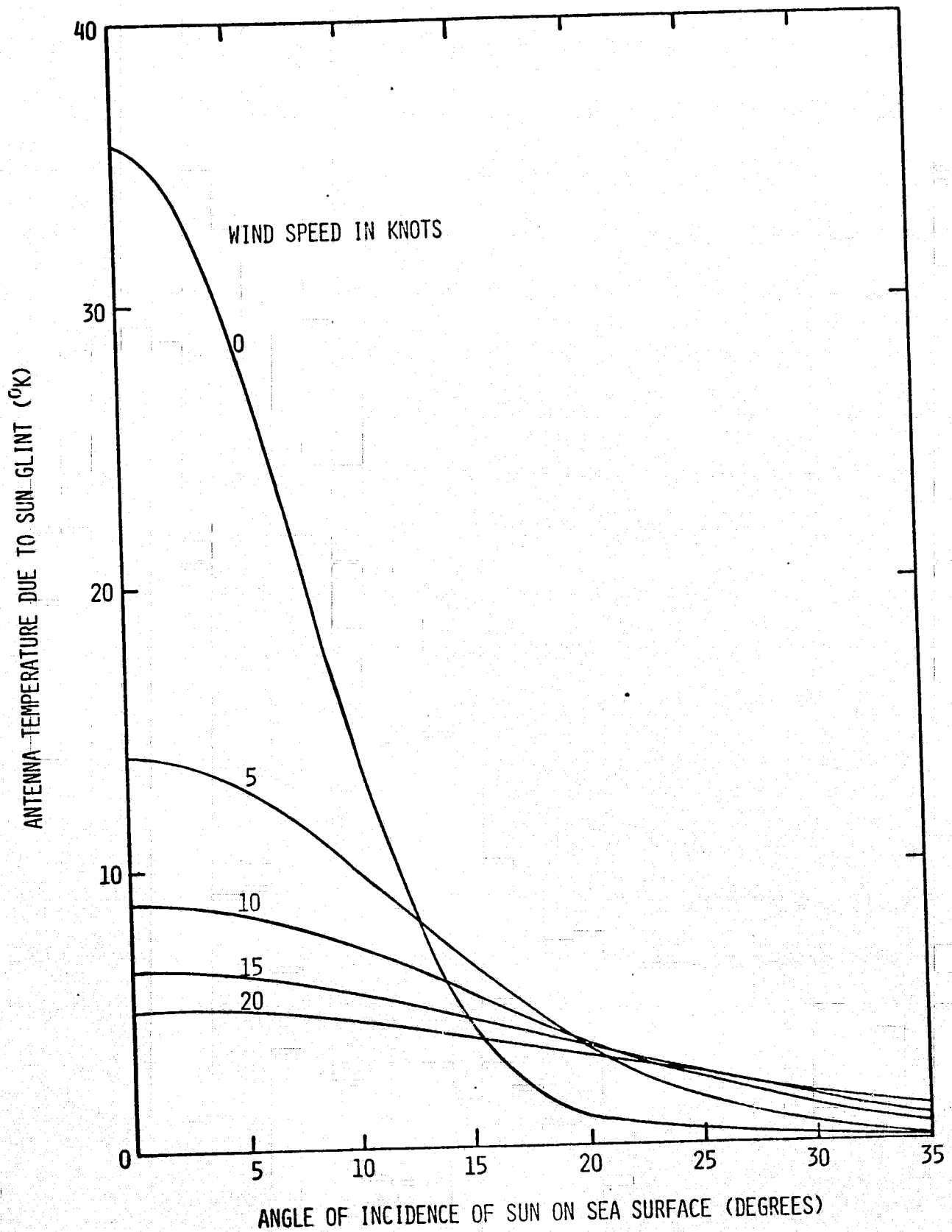
disportionately to the mean-square surface slope, its effective value decreases with decreasing observational frequency. The reduction at 1.4 GHz to one-third of the "optical" value is similar to the reduction measured by Cox and Munk for an oil slick covered surface compared to a clean surface. Since they calculated that an oil slick damped surface waves of 30 cm wavelength by a factor of 10 and that waves shorter than this were essentially eliminated, the sea surface at 1.4 GHz may very well be represented by the mean-square slope of a slick covered surface. Using a mean-square slope one-third of that given in equation (71) results in antenna temperature increases due to sun glint two to three times larger than the values given in Figure 11.

ANALYSIS OF S-194 DATA:

A compendium of all the S-194 measurements analyzed is presented in Table 2. This consists of 120 independent observations over 27 EREP passes and includes data over the Equatorial Pacific, North Pacific, North Atlantic, Equatorial Atlantic, and South Atlantic Oceans, the Gulf of Mexico, Caribbean Sea, the Great Lakes Region, the Southwest American Desert, and the Amazon River Panalopy. In general, over the open ocean regions a measured antenna temperature consists of an average over a statistically stable interval lasting for a period of several minutes. When the antenna response is varying rapidly as in Pass 14 over the Great Lakes and in regions of land-water boundaries, precise positions and

TABLE 2

SUMMARY OF S-194 DATA

DATE	SKYLAB PASS #	GMT	LAT. °N	LONG. °W	SUN ELEV. ANG. (°)	SALINITY PPT	SST °C	SPEED KTS	MEAS. ANT. TEMP (°K)	CALC. ANT. TEMP (°K)	ΔT MEAS. - CALC. (°K)	COMMENTS
6/5/73	5	18:04:00	24.5	92.0	88	36	27	12	114.2	103.7	--	Sun Glint
6/10/73	7	14:29:00	32.0	76.6	54	36	26	5	94.7	95.0	-0.3	Atlantic
		14:35:00	15.4	60.0	69	36	27	12	101.1	100.0	--	Sun Glint
		14:40:00	0.9	48.8	87	21	29	4	118.8	118.6	--	Sun Glint
6/11/73	8	15:19:00	33.0	96.8	48	--	--	--	251.9	---	--	South West Desert
		15:22:00	25.9	88.6	55	36	28	3	93.1	94.0	-0.9	Gulf of Mexico
		15:24:00	18.9	82.0	61	36	29	8	94.7	95.0	-0.3	Caribbean
		15:31:00	-1.3	66.0	62	--	--	--	271.6	---	--	Amazon Jungle
6/12/73	9	13:05:00	29.2	63.8	47	36	27	5*	93.7	94.8	-1.1	North Atlantic
		13:09:00	15.6	50.8	58	36	27	10*	95.3	95.9	-0.6	North Atlantic
		13:10:00	13.9	49.3	59	36	27	10*	96.2	95.9	.3	North Atlantic
		13:13:00	6.4	43.5	61	35.5	27	10*	96.9	96.2	.7	North Atlantic
		13:15:00	-0.2	38.5	60	36	28	5*	95.9	94.6	1.3	Equatorial Atlantic
		13:16:00	-2.4	36.8	59	36	28	5*	96.5	94.6	2.3	South Atlantic
		13:18:00	-9.8	31.2	55	36.5	27	10*	95.6	95.3	.3	South Atlantic
		13:19:00	-11.8	29.6	54	36.5	27	5	94.7	94.5	.2	South Atlantic
6/13/73	10	14:01:00	12.6	67.3	53	35.5	27	12	94.6	96.5	-1.9	Caribbean
8/4/73	13	17:09:00	49.7	160.6	16	33	12	5*	95.9	97.6	-1.7	North Pacific

TABLE 2 (continued)

DATE	SKYLAB PASS #	GMT	LAT. °N	LONG. °W	SUN ELEV. ANG. (°)	SALINITY PPT	SST °C	SPEED KTS	MEAS. ANT. TEMP (°K)	CALC. ANT. TEMP (°K)	ΔT MEAS.- CALC. (°K)	COMMENTS
8/4/73	13	17:09:00	50.2	149.2	24	33	13	5*	95.6	97.5	-1.9	North Pacific
		17:11:00	49.4	137.8	32	32	15	5*	96.7	98.7	-1.5	North Pacific
		17:13:00	33.0	96.0	68	--	--	--	270.2	---	--	South West Desert
		17:22:00	25.4	87.3	79	36	28	9	109.2	102.9	--	Sun Glint
		17:25:00	-1.3	65.2	65	--	--	--	274.5	---	--	Amazon Jungle
8/5/73	14	15:01:00.45	44.891	89.470	43	--	--	--	265.6	264.8	0.8	Wisconsin
		15:01:15.46	44.468	88.393	44	--	--	--	246.6	243.8	2.8	Wisconsin
		15:01:24.09	44.200	87.662	44	--	--	--	195.0	192.5	2.5	Wisconsin
		15:01:32.35	43.949	87.036	45	0	12	10	153.0	155.3	-2.3	Lake Michigan
		15:01:40.96	43.694	86.389	45	--	--	--	189.2	191.5	-2.3	Michigan
		15:01:49.56	43.486	85.744	46	--	--	--	242.7	244.0	-1.3	Michigan
		15:02:05.1	42.955	84.614	47	--	--	--	259.9	262.1	-2.2	Michigan
		15:02:24.95	42.334	83.186	48	--	--	--	229.4	232.0	-2.6	Michigan
		15:02:33.22	42.068	82.602	49	--	--	--	190.2	191.2	-1.0	Michigan
		15:02:41.16	41.812	82.059	49	0	23	10	173.0	172.0	-1.0	Lake Erie
		15:02:50.09	41.512	81.426	50	--	--	--	208.4	207.5	0.9	Ohio
		15:02:58.69	41.224	80.835	50	--	--	--	252.2	250.9	1.3	Ohio
		15:03:60.63	40.955	80.291	51	--	--	--	262.6	263.6	-0.9	Ohio
		15:03:37.39	39.887	78.237	53	--	--	--	266.5	266.1	0.4	Pennsylvania
		15:04:08.15	38.774	76.248	55	--	--	--	223.6	221.1	2.5	Maryland
		15:04:16.43	38.471	75.702	55	--	--	--	203.5	200.8	2.7	Maryland
		15:04:25.02	38.151	75.183	56	--	--	--	153.9	153.9	0	Maryland
		15:04:33.96	37.816	74.638	56	--	--	--	110.0	110.8	-0.8	Coast of Maryland

67

TABLE 2 (continued)

DATE	SKYLAB PASS #	GMT	LAT. °N	LONG. °W	SUN ELEV. ANG. (°)	SALINITY PPT	SST °C	SPEED KTS	MEAS. ANT. TEMP (°K)	CALC. ANT. TEMP (°K)	ΔT MEAS.- CALC. (°K)	COMMENTS
8/05/73	14	15:04:42.84	37.478	74.078	57	35.5	26	4	97.6	96.3	1.3	North Atlantic
		15:05:01.73	36.253	72.172	59	36.0	27	5	94.4	94.5	-0.1	North Atlantic
8/05/73	15	16:41:00	28.9	86.2	70	35.0	29	5*	104.2	98.8	---	Sun Glint
		16:46:00	15.0	73.0	87	36.0	28	5	104.4	107.8	---	Sun Glint
8/08/73	16	15:55:00	59.5	143.4	15	32.0	14	5*	97.4	98.1	-0.7	North Pacific
		15:57:00	47.9	133.3	22	32.0	16	5*	98.3	98.2	0.1	North Pacific
		16:05:00	32.8	100.3	50	---	--	--	283.3	---	---	Southwest Desert
		16:08:00	24.2	91.5	59	36.0	29	5	94.3	94.2	0.1	Gulf of Mexico
8/09/73	17	13:51:00	26.8	64.8	53	36.5	28	10*	92.4	93.7	-1.3	North Atlantic
		13:59:00	4.7	45.8	70	36.0	27	5*	93.9	94.8	---	Sun Glint
9/02/73	23	17:55:30	10.7	58.6	60	32.0	28	5*	100.0	99.8	0.2	Off Northeast Coast of Venezuela
		17:55:40	11.1	58.4	59	32.0	28	5*	99.0	98.0	1.0	North Atlantic
		17:56:20	13.1	56.7	58	35.0	28	20	98.1	97.9	0.2	North Atlantic
		17:57:10	15.7	54.6	55	36.0	28	30	99.0	98.8	0.2	Closest approach to tropical storm Christine
		17:57:20	16.3	54.1	54	36.0	28	25	98.1	98.0	0.1	North Atlantic
		17:58:00	18.0	52.6	53	36.0	28	10	95.9	95.6	0.3	North Atlantic
		17:59:00	21.1	49.9	49	36.0	28	5	94.9	94.8	0.1	North Atlantic
		18:00:00	23.4	47.6	47	37.0	28	5	94.0	94.1	-0.1	North Atlantic

TABLE 2 (continued)

DATE	SKYLAB PASS #	GMT	LAT. °N	LONG. °W	SUN ELEV. ANG. (°)	SALINITY PPT	SST °C	SPEED KTS	MEAS. ANT. TEMP (°K)	CALC. ANT. TEMP (°K)	ΔT MEAS.- CALC. (°K)	COMMENTS
9/09/73	29	19:09:00	12.8	118.0	79	33.0	25	0	115.4	111.2	---	Sun Glint
		19:27:00	50.1	48.0	20	32.0	11	14	98.4	99.6	-1.2	North Atlantic
		19:30:00	49.4	30.7	9	35.5	16	11	98.1	97.8	0.3	North Atlantic
9/10/73	31	20:05:00	29.4	121.2	64	34.0	20	5*	98.0	97.5	0.5	North Pactific
9/13/73	38	18:09:00	50.2	48.8	30	33.0	10	10*	99.9	98.6	1.3	North Atlantic
		18:10:00	50.1	44.0	28	34.5	13	10*	100.8	98.1	2.7	North Atlantic
		18:12:00	49.1	32.8	21	35.0	17	10*	100.1	97.9	2.2	North Atlantic
9/14/73	40	17:05:00	5.4	123.3	44	35.0	27	5*	99.5	95.4	-0.9	Equatorial Pacific
		17:08:00	14.2	116.3	51	34.0	28	5*	94.7	95.9	-1.2	North Pacific
		17:09:00	18.9	112.4	53	34.0	28	5*	93.8	95.9	-2.1	North Pacific
		17:30:00	48.0	21.4	21	35.5	16	10*	94.3	97.7	-3.4	North Atlantic
9/15/73	43	18:01:00	22.2	128.2	50	34.0	23	6	98.3	96.8	1.5	North Pacific
		18:02:00	25.5	125.0	51	34.0	22	6	98.3	96.9	1.4	North Pacific
		18:04:00	30.4	119.7	52	34.0	19	8	100.2	97.2	3.0	North pacific
12/04/73	60	16:45:00	49.3	150.3	-9	33.0	6	5*	95.3	97.4	-1.9	North Pacific
1/04/74	73	19:40:00	47.7	13.7	23	35.5	12	10*	96.2	96.6	-0.4	North Atlantic
1/06/74	74	17:57:00	27.2	88.1	40	36.0	23	5*	94.5	95.6	-1.1	Gulf of Mexico
		17:58:00	28.5	86.7	39	36.0	21	5*	95.5	95.9	-0.4	Gulf of Mexico
		18:07:00	47.9	48.6	10	34.0	2	10*	96.4	97.6	-1.2	North Atlantic
		18:11:00	50.2	26.2	-3	34.0	2	10*	97.0	97.6	-0.6	North Atlantic

TABLE 2 (continued)

DATE	SKYLAB PASS #	GMT	LAT. °N	LONG. °W	SUN ELEV. ANG. (°)	SALINITY PPT	SST °C	SPEED KTS	MEAS. ANT. TEMP (°K)	CALC. ANT. TEMP (°K)	ΔT MEAS.- CALC. (°K)	COMMENTS
1/06/74	74	18:13:00	49.5	14.8	-9	35.5	11	10*	96.1	97.7	-1.6	North Atlantic
1/07/74	76	17:14:00	25.4	85.3	42	36.0	23	10*	96.9	96.7	0.2	Gulf of Mexico
		17:24:00	46.7	48.7	16	33.0	1	10*	97.6	97.8	-0.5	North Atlantic
1/08/74	78	16:29:00	19.8	85.7	43	36.0	23	5*	95.5	95.6	-0.1	Gulf of Mexico
		16:32:00	27.8	77.9	38	36.5	24	4	94.2	95.3	-0.9	North Atlantic
		16:34:00	31.7	73.4	36	36.5	24	4	95.8	95.3	0.5	North Atlantic
		16:35:00	34.9	69.1	33	36.5	20	4	95.8	95.9	-0.1	North Atlantic
		16:36:00	37.3	65.6	30	36.5	20	10	96.5	96.9	-0.4	North Atlantic
		16:37:00	39.2	62.5	28	36.0	17	10*	98.4	97.4	1.0	North Atlantic
		16:38:00	40.6	59.8	27	36.0	13	10*	97.1	97.5	-0.4	North Atlantic
		16:39:00	43.2	54.2	23	34.0	3	10*	97.0	97.7	-0.7	North Atlantic
		16:40:00	44.4	51.3	22	33.0	3	7	96.1	97.4	-1.3	North Atlantic
		16:41:00	47.6	40.4	18	35.5	12	10*	94.8	97.7	-2.9	North Atlantic
1/09/74	79	15:51:00	31.1	69.4	35	36.5	23	8	96.4	96.1	0.3	North Atlantic
		15:52:00	33.8	62.1	33	36.5	20	6	97.3	96.6	0.7	North Atlantic
		15:55:00	29.6	56.9	28	36.0	14	30	101.5	100.7	0.8	North Atlantic
		15:57:00	44.4	46.4	23	36.0	6	48	103.0	103.3	-0.3	North Atlantic
		15:58:00	46.3	40.9	20	36.0	12	48	103.9	102.5	1.4	North Atlantic
		15:59:00	47.2	37.5	18	36.0	12	48	103.6	102.5	1.1	North Atlantic
		16:00:00	48.7	30.4	15	35.5	10	20	100.5	99.3	1.2	North Atlantic

TABLE 2 (continued)

DATE	SKYLAB PASS #	GMT	LAT. °N	LONG. °W	SUN ELEV. ANG. (°)	SALINITY PPT	SST °C	SPEED KTS	MEAS. ANT. TEMP (°K)	CALC. ANT. TEMP (°K)	ΔT MEAS.-CALC. (°K)	COMMENTS
1/09/74	79	16:02:00	50.1	18.4	9	35.5	10	10*	99.2	97.7	1.5	North Atlantic
		16:04:00	50.2	11.0	6	35.5	11	13	97.9	97.8	0.1	North Atlantic
1/11/74	81	17:49:00	46.8	24.2	6	36.0	12	10*	97.7	97.5	0.2	North Atlantic
1/27/74	92	12:18:00	13.3	143.4	53	34.0	26	14	99.3	98.7	0.6	North Pacific
		12:20:00	19.5	138.1	49	34.0	22	20	100.3	100.4	-0.1	North Pacific
		12:22:00	23.3	134.6	46	34.0	21	23	99.3	100.1	-0.8	North Pacific
		12:23:00	27.4	130.4	42	34.0	18	17	99.0	99.4	-0.4	North Pacific
		12:43:00	44.7	36.6	22	36.0	14	45	104.3	103.0	1.3	North Atlantic
		12:46:00	38.5	23.4	31	36.0	17	31	100.5	100.6	-0.1	North Atlantic
		12:47:00	35.8	19.1	35	36.0	17	16	99.2	98.3	0.9	North Atlantic
1/29/74	95	17:39:00	24.0	90.4	47	36.0	25	11	97.9	96.5	1.4	North Atlantic
		17:49:00	-3.3	68.3	69	---	--	--	270.3	---	---	Amazon Jungle
1/30/74	96	16:44:00	49.6	139.0	-2	33.0	6	17	98.3	99.3	-1.0	North Pacific
		16:45:00	48.7	132.4	3	33.0	7	11	99.1	98.4	0.7	North Pacific
		16:54:00	33.1	96.0	34	---	--	--	198.3	---	---	Southwest Desert
		16:57:00	24.7	86.3	45	36.0	26	5	98.6	95.2	3.5	North Atlantic
		16:59:00	16.8	79.1	55	36.0	26	18	99.5	97.4	2.1	North Atlantic
		17:06:00	-1.3	65.0	72	---	--	--	275.1	---	---	Amazon Jungle

71

TABLE 2 (continued)

DATE	SKYLAB PASS #	GMT	LAT. °N	LONG. °W	SUN ELEV. ANG. (°)	SALINITY PPT	SST °C	SPEED KTS	MEAS. ANT. TEMP (°K)	CALC. ANT. TEMP (°K)	ΔT MEAS.- CALC. (°K)	COMMENTS
2/01/74	98	16:51:00	50.1	161.6	-14	33.0	5	5*	98.5	97.1	1.4	North Pacific
		16:53:00	48.7	146.7	-4	33.0	7	25	99.2	100.1	-1.6	North Pacific
		16:56:00	45.8	134.8	5	33.0	9	20	99.2	100.1	-0.9	North Pacific

* Denotes ground truth data taken more than five hours away form measurement time.

times are recorded and averages of only a few seconds duration are used.

The first column of Table 2 gives the date that the measurement was taken. The second column gives the Skylab pass number using the continuous numbering system beginning with Skylab II rather than the alternative system, occasionally used elsewhere, which starts anew at the beginning of each Skylab mission. The sun elevation angle is the complement of the angle of incidence of the sun's rays at the point directly below the S-194 antenna.

Salinity measurements in parts per thousand were obtained from the hundred year averages compiled by the U.S. Naval Oceanographic Office (23), and as given by Sverdrup, Johnson and Fleming (24). These values, while accurate on the average, may not apply in specific cases. For example, a recent heavy rain can result in significant temporary local variations in the surface salinity. It is not likely that this would result in an appreciable effect at 1.4 GHz however, except under unusually heavy rain conditions, since the skin depth at 25°C sea temperature increases from 0.9 cm for 35 PPT salinity to over 10 cm for fresh water. Therefore, S-194 would respond to water well below the thin fresh water surface. Turbulance and mixing would, of course, tend to prevent a significant salinity gradient with depth. In addition, the footprint of the S-194 on the earth's surface

73

has a 60 nautical mile diameter, so that it would be necessary for the heavy rainfall to occur over a large area for its effect on the antenna temperature to be noticeable.

Sea temperature measurements were obtained from the Fleet Numerical Weather Central (FNWC), Monterey, California, except for the Great Lakes measurements which were provided for Pass 14 by the Detroit Office of NOAA. Wind speed in knots was obtained from the Daily Weather Maps produced by NOAA (e.g. 25) for the Great Lakes. Over the ocean wind speed values came from FNWC. Wind speed value labeled with an asterisk are estimates using data taken more than five hours away from the measurement time of the antenna temperature.

The measured antenna temperature recorded in Table 2 incorporates the corrections applied to the electronics box constants C_2 and C_4 as discussed previously. The calculated antenna temperature is the output of program ANTTEMP and incorporates the specification of sea temperature, sea salinity, wind speed, and the atmospheric conditions obtained from all available ground truth. Although antenna temperatures were computed for data points with sun elevation angles in excess of 65° (incidence angles less than 25°), the measured antenna temperature minus the calculated antenna temperature (ΔT) was not calculated and the data were not used in any further analysis due to the extreme sensitivity of the antenna temperature to wind speed at these low solar incidence angles as shown in Figure 11. The "comment" column identifies

74

sun glint problems and gives the general location of each measurement.

The first objective in the analysis of S-194 data is to examine those measurements taken over clear, calm ocean conditions to confirm the reduction and analysis techniques under the most ideal ocean environment before proceeding to more complex conditions. Three areas with calm seas, defined as wind speed less than or equal to five knots, minimum atmospheric loss and with very good ground truth available were selected. One area is in the South Atlantic and was measured during Pass 9 on 6/12/73. The other two areas are in the North Atlantic and were measured during Pass 23 on 9/2/73. The agreement between measured and calculated antenna temperatures was excellent as summarized below:

DATE	SL PASS	MEASURED ANT. TEMP.	CALCULATED ANT. TEMP.
6/12/73	9	94.7	94.5
9/2/73	23	94.9	94.8
9/2/73	23	94.0	94.1

We feel that this confirms the accuracy of the calibration and analysis techniques and establishes the basis for the investigation of more complex environments.

The second objective in the analysis is to devise a method for computing the antenna temperature when the beam includes a land-water interface or other such areas of rapidly changing signal. The half-power beam-width of the

75

S-194 antenna is 15°. As can be seen in Figure 3, the main-beam, defined as the beam included within the first null at 20° off the main-beam axis, contains 98% of the antenna solid angle. Further, 99% of the power received by S-194 is included within a 41° angle from nadir. A program MAPS was written to map the S-194 beam pattern out to 41° off nadir onto the earth's surface. MAPS approximates the beam pattern by a grid of 1728 points. The height above the earth's surface of Skylab and the latitude and longitude of the nadir point are inputs to MAPS. Longitude and latitude is computed every ten degrees in azimuthal angle and every half degree angle off nadir out to eighteen degrees (97.5% power included) then every two degrees out to forty-one degrees. From the output of MAPS superimposed on a world map each point was then identified as either being on land or water and inputs to ANTTEMP adjusted accordingly.

The first such model was made of an arbitrary straight line interface between land at a brightness temperature of 276.5°K and the ocean at a brightness temperature of 96.2°K to examine the effects of worst case pointing error on antenna temperature. A study of the Skylab attitude pointing error which used data from the Skylab camera systems provided 3σ uncertainties of 2.5° for EREP Passes 1 through 20 and 0.8° for all subsequent EREP passes. These uncertainties correspond to a worst case error of the center of the antenna footprint on the earth's surface of 10.2 nautical

miles for EREP Passes 1-20 and 3.2 nautical miles for subsequent passes. If it is assumed that the nadir look angle is exactly on the interface, a pointing error of 2.5° will result in an error in measured antenna temperature of 27.4° (a 14.7% error); and a pointing error of 0.8° will result in an error in the measured antenna temperature of 7.1°K (a 3.8% error). It is thus clear that pointing error can be a significant source of error in measured antenna temperature if the main beam of S-194 includes such a land-water interface.

Such an interface occurred frequently during Pass 14, Ground Track 61/62, August 5, 1973. This Pass started near Seattle, Washington; traversed parts of Lake Michigan and Lake Erie and proceeded into the Atlantic Ocean. Figures 12, 13, 14, and 15 show the integration points of the S-194 main beam mapped onto selected target areas in Pass 14. In order to display the output of MAPS with the minimum of clutter, the program was altered to plot points in azimuth every thirty degrees for the first five degrees in angle off nadir. Figure 13 represents the beam pattern mapped on the earth's surface at a nadir point 42.334 degrees North Latitude and 83.186 West Longitude. The Great Lakes -- Michigan, Huron, Erie, and Ontario -- are represented to scale. It can easily be seen that the true contour of the northwest shoreline of Lake Erie and the southern shoreline of Lake Huron must be accurately represented for the output of ANTTEMP to be consistent with the measured antenna
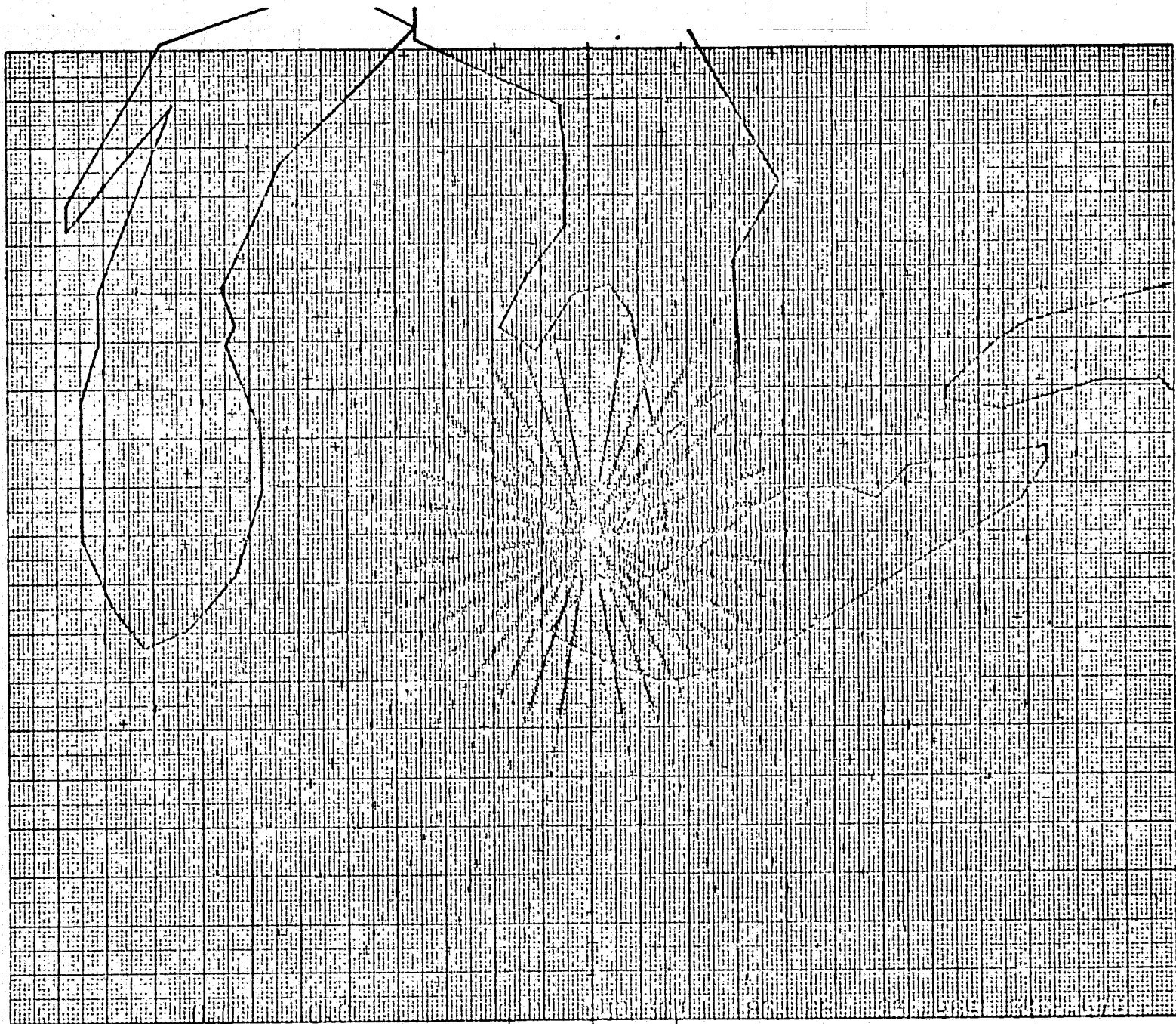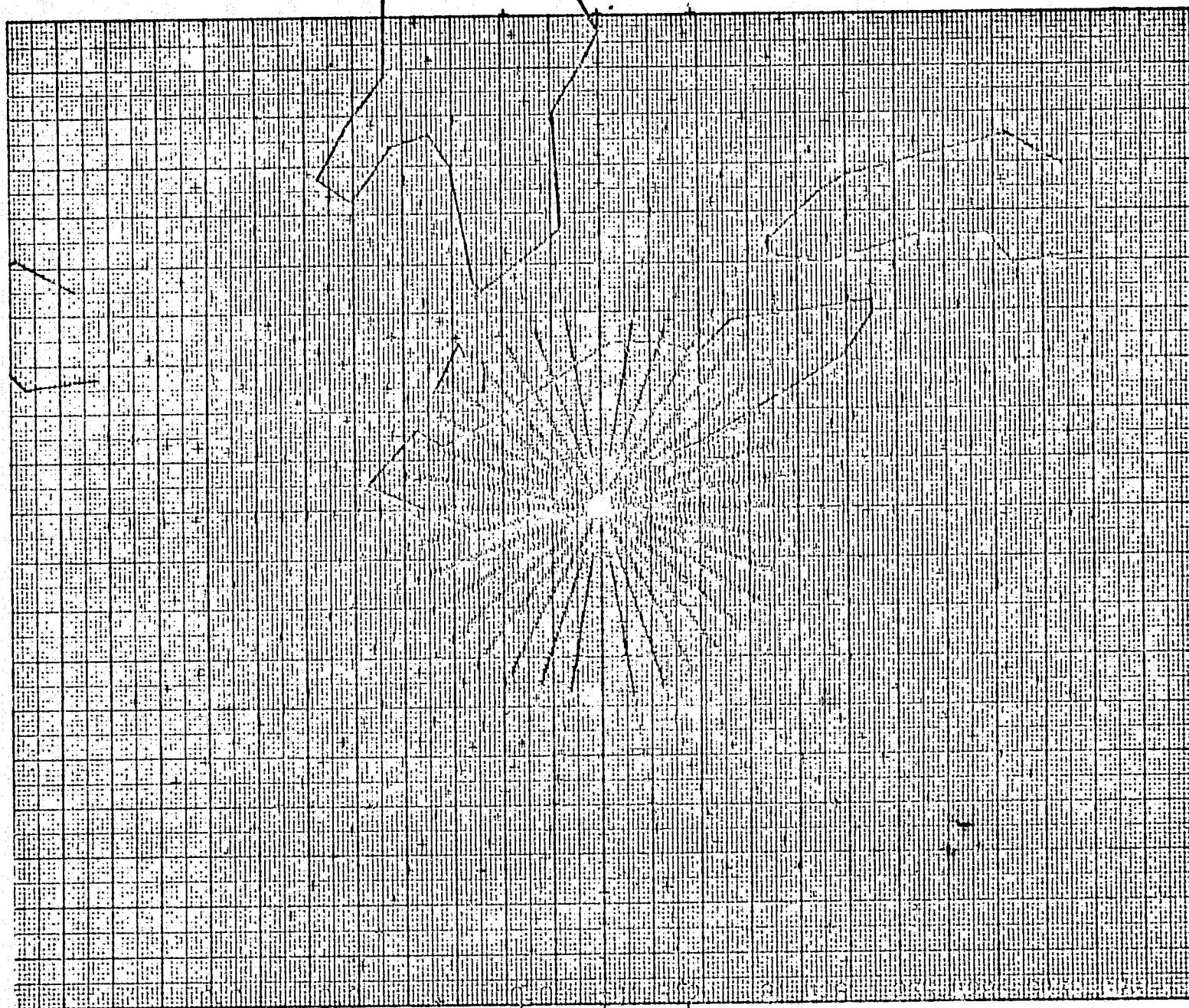
Figure 12

Figure 13

Figure 14

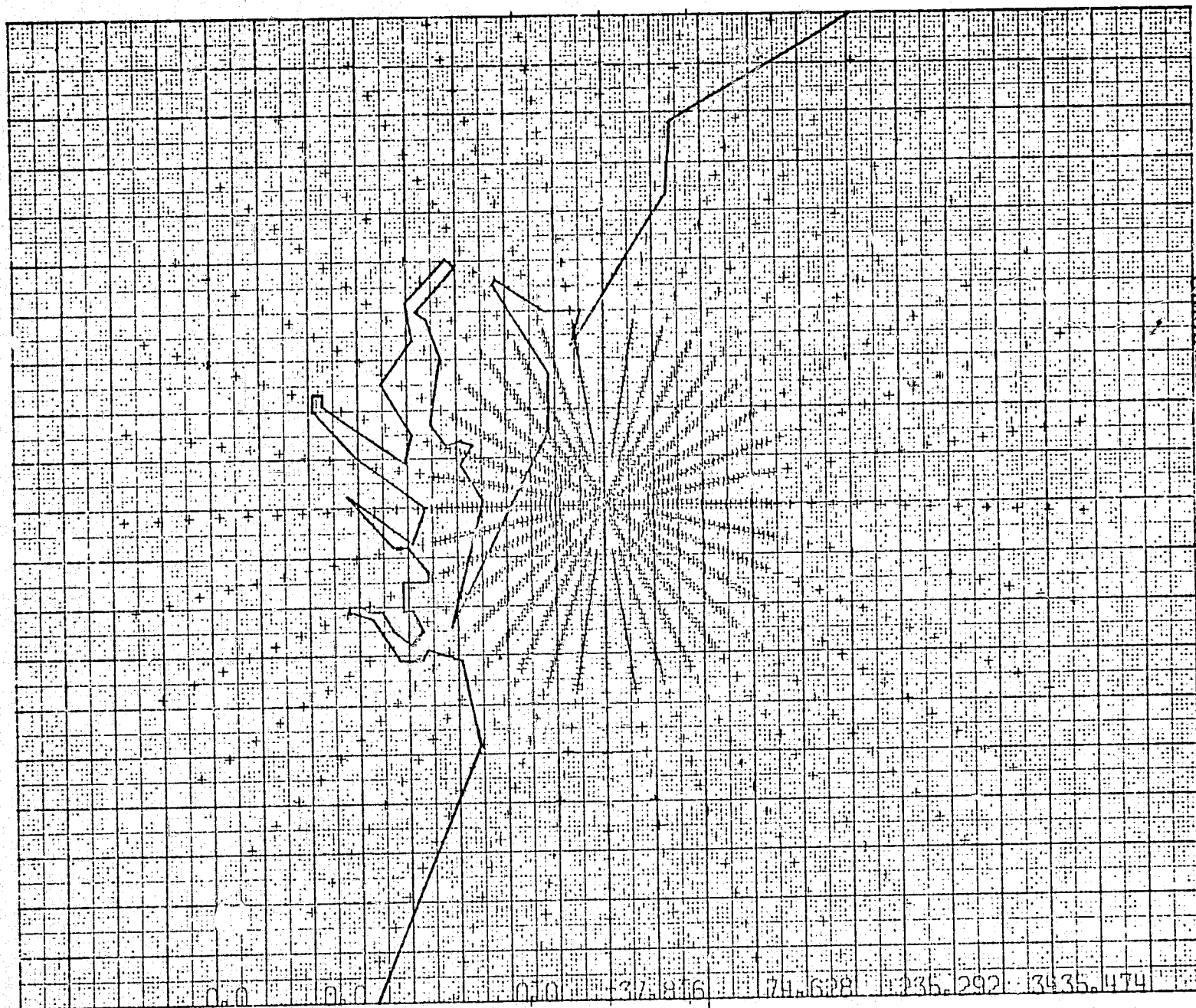0.0   0.0   0.0   37.816   74.628   135.292   3435.474
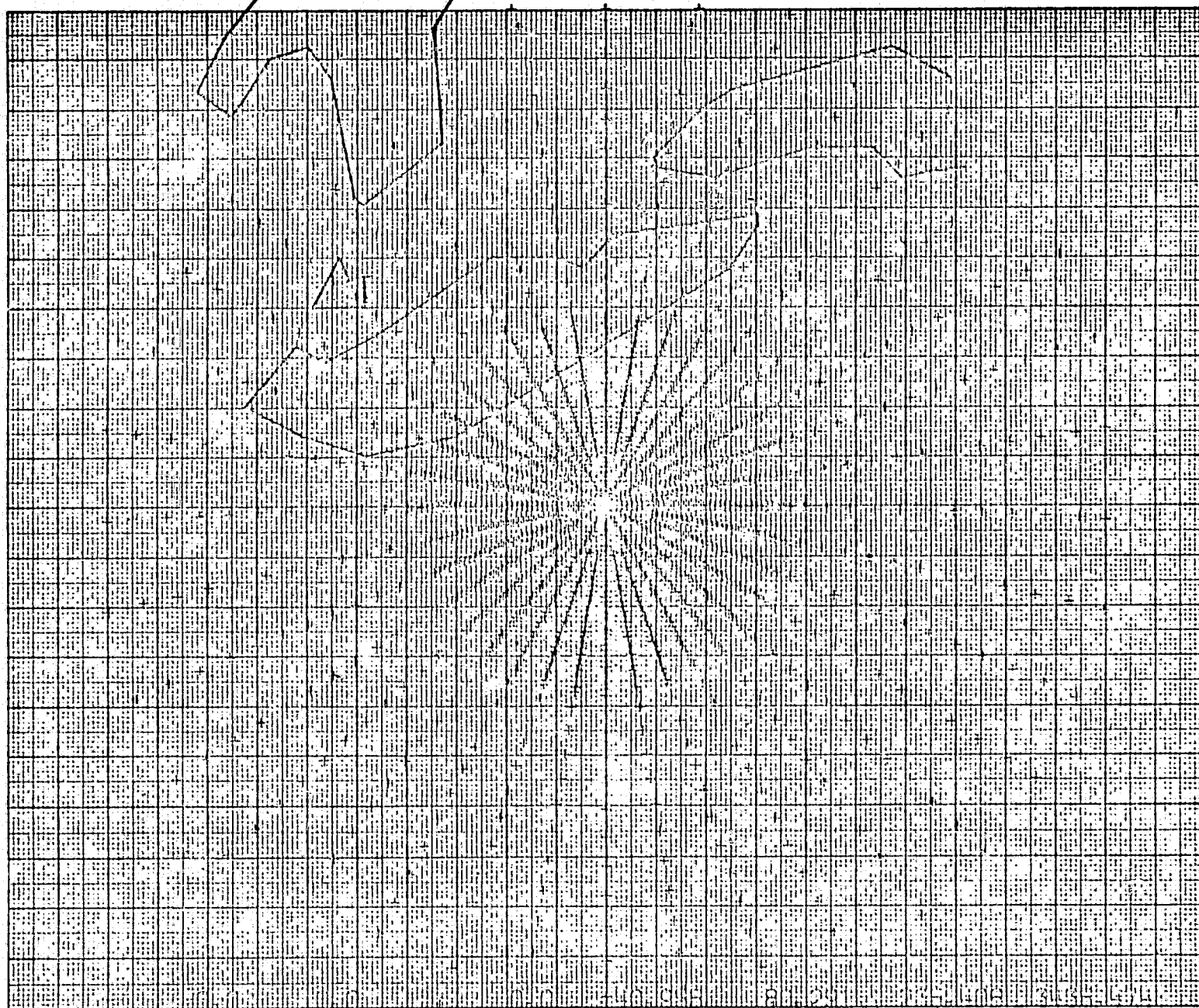
Figure 15

temperature. Figure 14 represents the same scene but with the beam pattern advanced along the ground track one and one-half beam-widths to 41.512 North Latitude and 81.426 West Longitude. Here only the contour of Lake Erie is truly significant to the input for ANTTEMP. Figure 15 shows the scene with the beam pattern one beam-width advanced from Figure 14. Note that now it is the southeast shoreline of Lake Erie that is most critical. Figure 16 incorporates a map of the Chesapeake Bay region. We found it was necessary to make this map quite detailed, to include, for instance, the outlets and major portions of the Potomac, Choptank, Rappahannock, and James River, in order to correctly model the area. Similar complex bay areas would have to be modeled with equal precision.

The antenna temperatures calculated for Pass 14 using MAPS at the four points modeled in Figures 12, 13, 14, and 15, as well as for 16 other points, are shown in Figure 16. The calculated points are represented by the open circles and the solid line represents the actual S-194 measurements. An approximate topological cross-section along Pass 14 with an exaggerated vertical scale is shown along the bottom of the figure to identify the topological feature being overflown. The half-power antenna footprint on the surface is the same size as the Lake Michigan cross-section along the ground track. Since the footprint is comparable in size with Lakes Michigan and Erie, and with the Chesapeake Bay, a significant portion of the antenna beam is filled by land for all inland
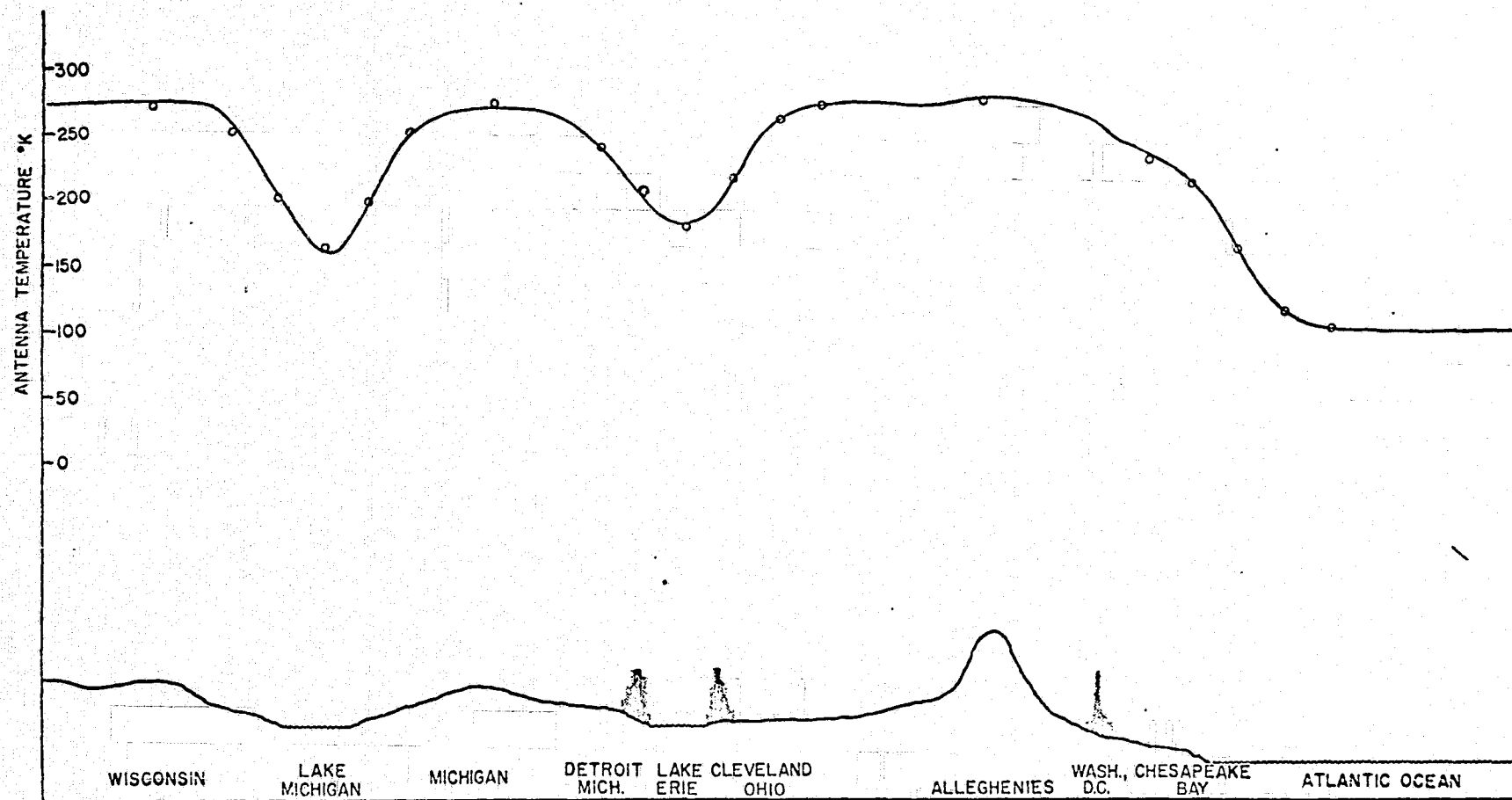
Figure 16

water areas in Pass 14. Since the brightness temperature of
the land is 266°K, more than 150°K above the brightness
temperature of water, the antenna temperature is significantly
increased if even a small portion of the beam is filled by
land. For example, if there had been no land in the antenna
beam, antenna temperatures 44.8°K and 58.6°K lower than the
minimum actually measured would have been measured for Lakes
Michigan and Erie, respectively. The brightness temperature
for land of 266°K was obtained from the measured antenna
temperature west of Lake Michigan where the beam was completely
filled by land. This value for land was used in all of the
model calculations for the entire pass. Due to the amount
of land in the antenna beam, the effects of salinity of
about 10°K between the lakes and the ocean are reduced by
about 30% to 7°K. This change due to salinity is significant
and well above the measurement error. Thus, even with the
large land effect, the salinity difference between the lakes
and ocean are detectable from the S-194 measurements. The
antenna temperature measurements and calculations are in
excellent agreement with a mean difference of 0.063°K and a
standard deviation of 1.8°K. This indicates that accurate
model calculations can be made even in complex land-water
regions where the antenna temperature is changing rapidly.

Since the third objective of this investigation is to
measure the effects of salinity, it was hoped that a study
of Pass 7 from the North Atlantic to the South Atlantic,

passing within two degrees of longitude of the Amazon River outlet, would show the change in ocean salinity due to the fresh water outflow from the Amazon River. Unfortunately, sun elevation angles were close to 90° during the critical part of Pass 7 and the measured antenna temperature is not reliable because of the uncertainty in the large possible correction to it by sun glint. Salinity variations of from at least 10 to 15 PPT near the mouth of the Amazon River to 36 PPT in the Atlantic Ocean are to be expected during the rainy season at this time of year. This salinity variation corresponds to an expected antenna temperature increase of as much as 20°K. Although antenna temperatures of 119°K in the Amazon mouth and 95°K in the ocean, an increase of 24°K, were measured, this increase cannot definitely be regarded as resulting from salinity effects due to the uncertainty in the sun glint correction.

Since salinity changes of up to 5 PPT do occur from point to point over the open ocean, it is possible to look for the salinity effect in the ocean data. In order to do this, it is necessary to remove the effects due to variations in sea temperature and marine wind speed along the ground track. The dependence of antenna temperature on salinity was computed using all of the available ocean data. The data were normalized using the model dependence for sea temperature and wind speed, to an ocean temperature of 25°C and a wind speed of 5 knots and are shown in Figure 17. The
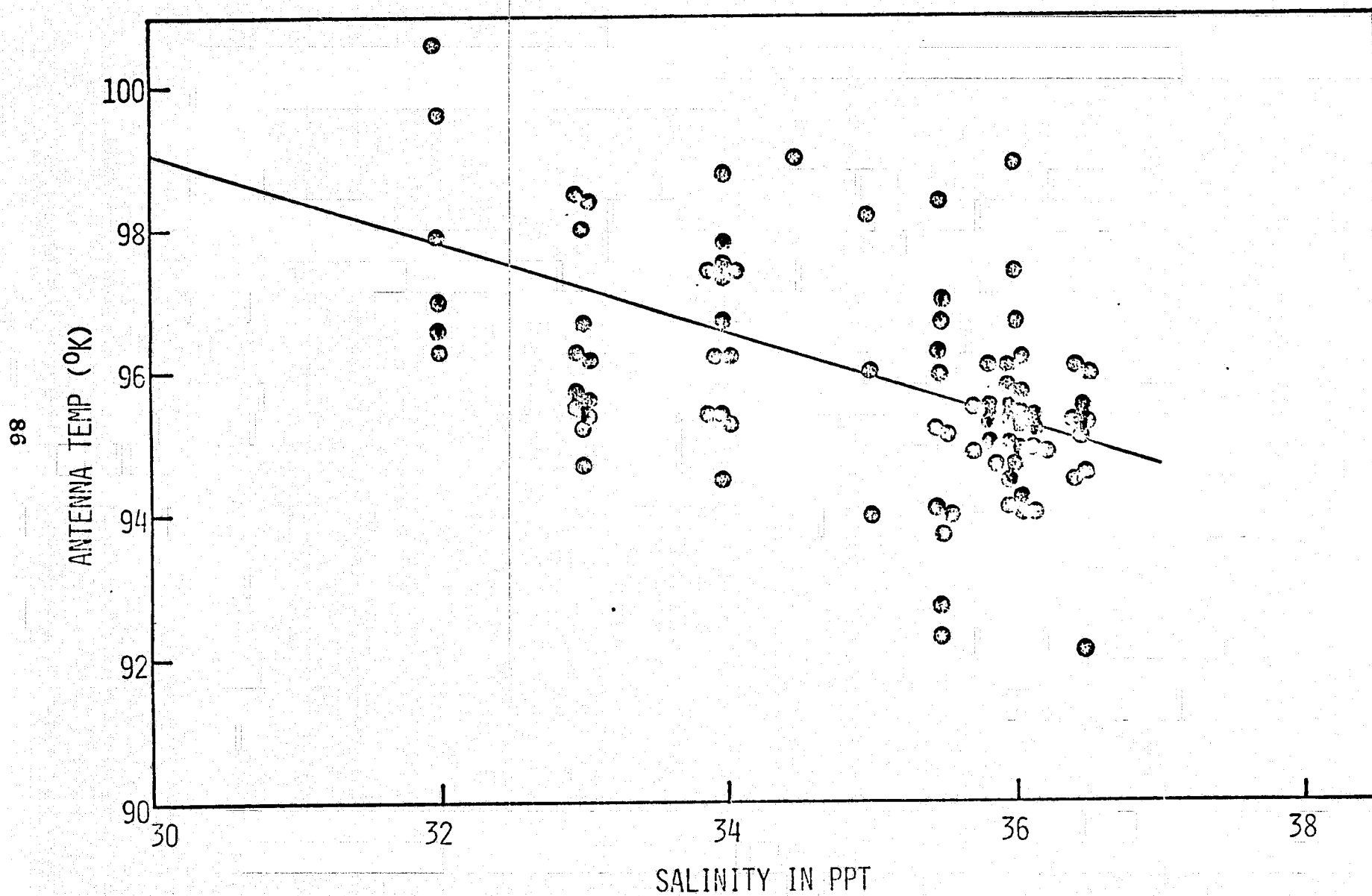
Figure 17

dots are the normalized data points and the solid line represents the theoretical dependence of antenna temperature on salinity. Although most of the data are clustered about 36 PPT, and there is only a small range in salinity, the measurements are quite consistent with the theoretical model.

The fourth objective is to examine the effects of changing thermodynamic water temperature on the antenna temperature measurements. In order to perform this analysis, it was first necessary to remove the influence of changing wind speed and sea surface salinity by normalizing all data points to a wind speed of 5 knots and a salinity of 36 PPT. All of the ocean measurements are used. Figure 18 is a plot of antenna temperature vs. sea temperature where the dots are the normalized measurements and the solid line represents the theoretical dependence. There is a large change in sea temperature, ranging from near 0°C to nearly 30°C. Only a small change in antenna temperature is expected even for this 30°C change in sea temperature. The measurements confirm this result and are in good agreement with the theoretical model. S-194 is clearly not the instrument to be chosen for remote determination of sea temperature.

The fifth objective is to consider the effects of wind speed, sea surface roughness, and foam coverage on the measured antenna temperature. On September 2, 1973, during Pass 23, Skylab passed over a portion of Tropical Storm
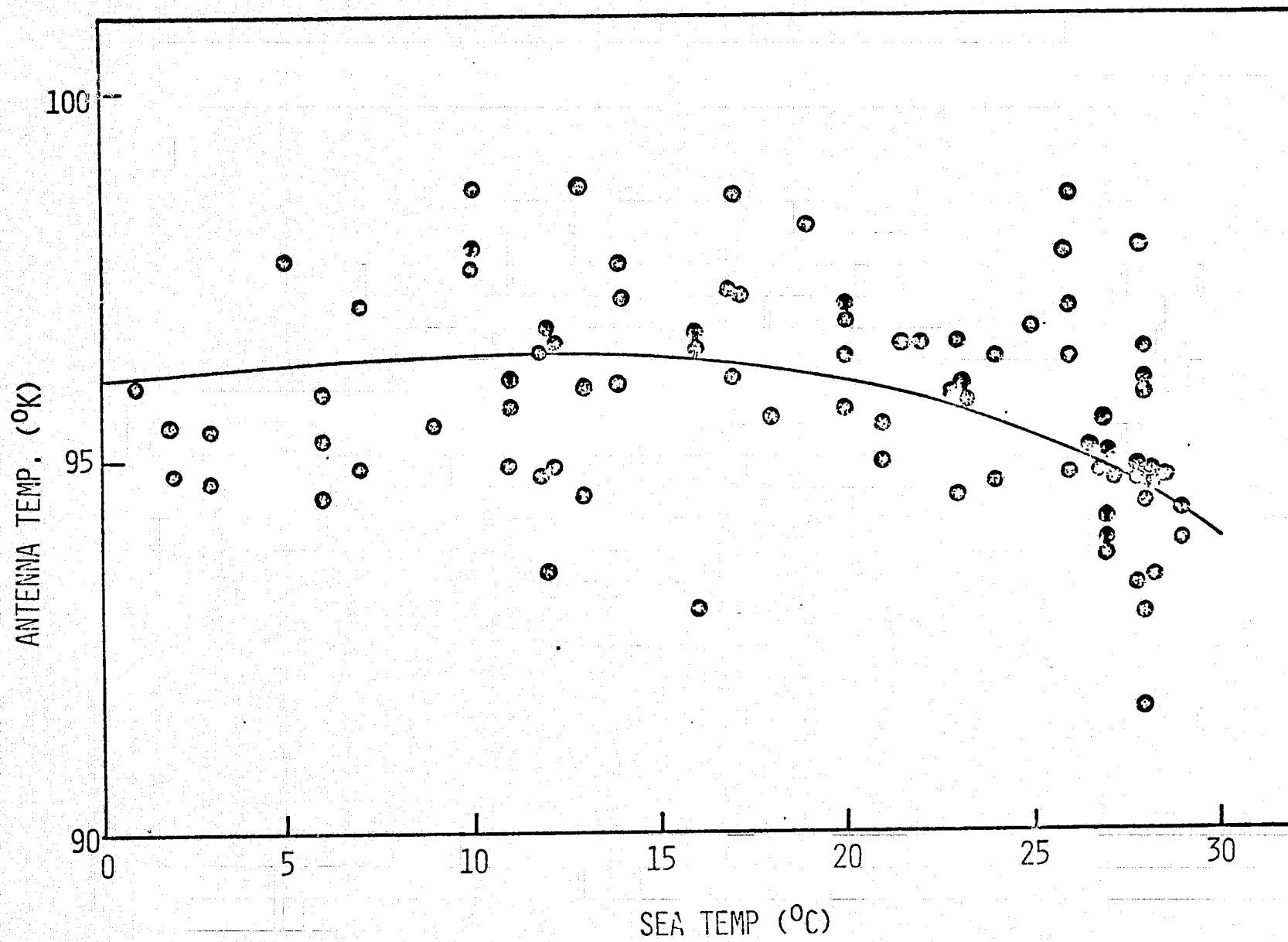
Figure 18

Christine. The excellent ground truth available for this storm makes it a good target of opportunity for the study of the effects of high winds and ocean roughness. Figure 19 shows the ground track of Pass 23, through an outline representation of the storm area, with a graph of measured antenna temperature superimposed on it. The solid outline encompasses the center of the storm and heaviest cloud cover. The dotted line shows the extent of associated, but lighter, cloud cover. As can b seen, the S-194 footprint never passes through the most i tense part of the storm. In addition, the effect of high wi ds is somewhat hidden by the circumstance that the S-194 foc print was moving from an area of 32 PPT salinity at the left end of the track to an area of 37 PPT salinity on the other side of Christine as can be seen in Table 2. This change in salinity results in a 5.7°K decrease in the calculated antenna temperature in going from one side of Christine to the other. This is accurately reflected in the S-194 measurements. The increase in antenna temperature in the vicinity of Christine is about 3 to 5°K. This increase may result not only from roughness effects but also may in part be due to very heavy rain and local decreases in surface and near-surface salinity resulting from the rain. Thus, the contribution due to wind speed effects is difficult to assess. The increase of 3 to 5°K is consistent with a wind speed increase of from 20 to 30 knots above that outside the storm area. This is consistent with the position of the ground track along the outer edge of the storm.
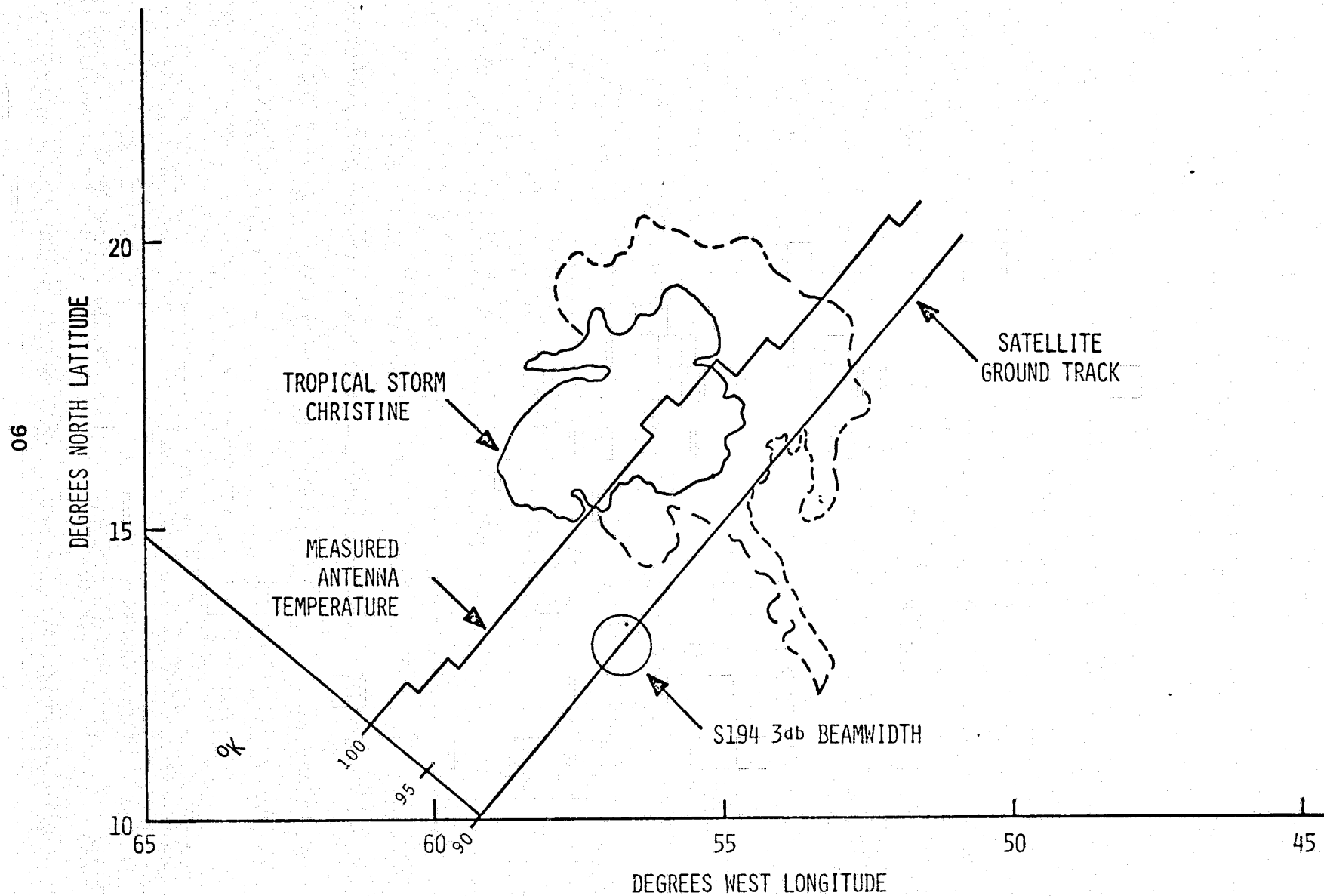
Figure 19

During Pass 79, over the North Atlantic, wind speeds of
from 6 knots up to 48 knots were reported by FNWC. Since
the salinity variation is only ±0.5 PPT over the ground
track from 31.1 North Latitude, 69.4 West Longitude to 48.7
North Latitude, 30.4 West Longitude, the effects of high
wind speed on antenna temperature is more easily discerned
than during Pass 23. There is an unmistakeable antenna
temperature increase of nearly 7°K corresponding to the wind
speed increase of 40 knots. This dependence of about
0.17°K/knot is very close to the value of 0.16°K/knot expected
as discussed earlier.

In order to more fully investigate the wind speed
effect, all of the ocean data where the wind speed was well
known, i.e. where no asterisk appears in Table 2, and no sun
glint was present, were adjusted to remove the effects of
variations in salinity and sea surface temperature. Figure
20 is a plot of antenna temperature versus wind speed for
these data where all of the data have been normalized to
25°C sea temperature and 36 PPT salinity using the theoretical
dependence on sea temperature and salinity. The solid line
in Figure 20 is the straight line which best fits the data
as determined by linear regression analysis. The correlation
coefficient of 0.87 indicates a very significant wind speed
dependence. This is also apparent from the good fit of the
data to the regression line over the considerable range in
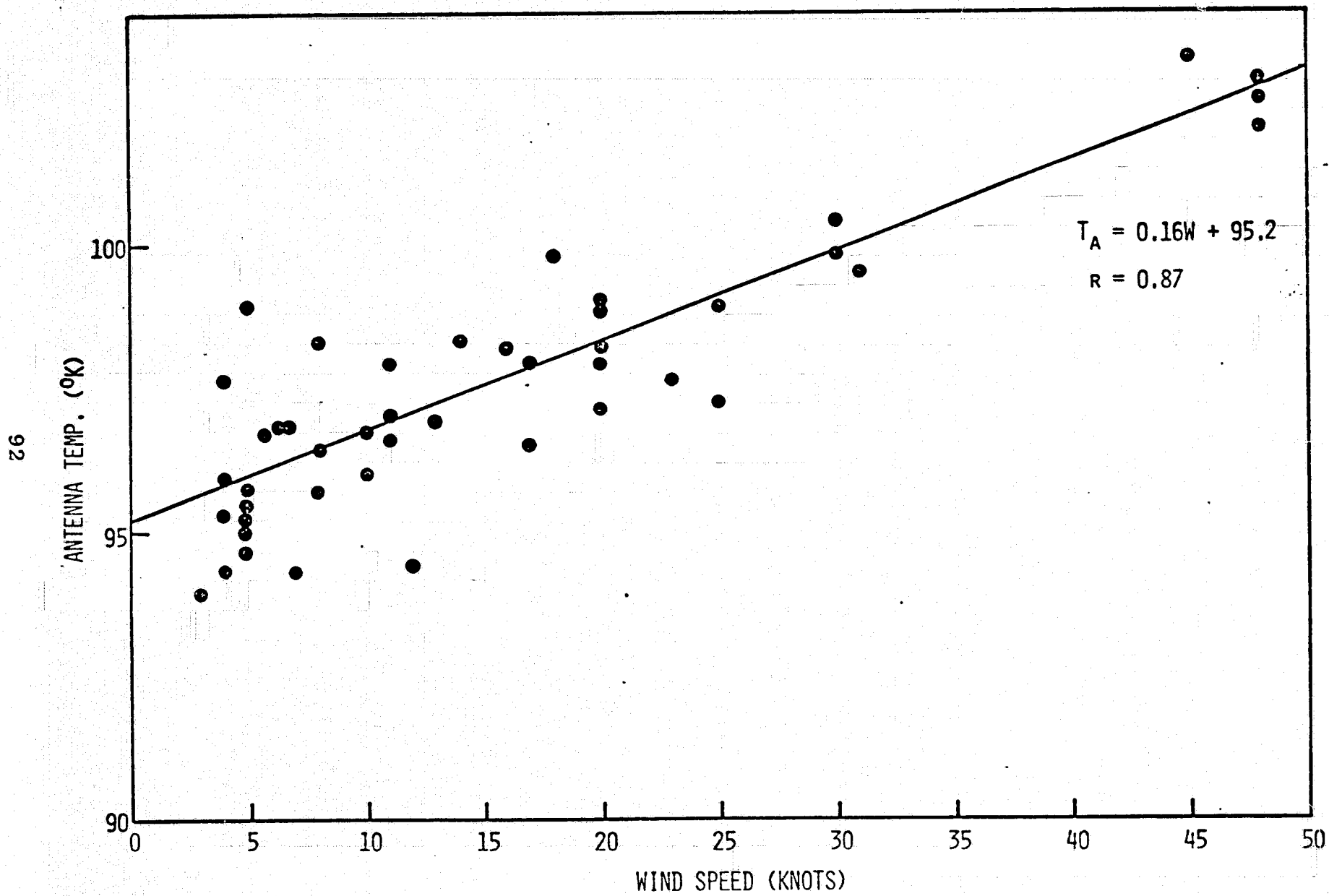wind speed of from 3 to 48 knots and corresponding change of

91

Figure 20

about 15°K in antenna temperature. The adjustment of the data to 25°C sea temperature and 36 PPT salinity, required only relatively small changes in antenna temperature. The total range in sea temperature over the data of from 3 to 29°C required less than a 2°K adjustment, and the salinity range of from 32 to 37 PPT required less than a 6°K adjustment in the antenna temperature. Further, any possible atmospheric differences over the data could result in variations of at most a few tenths of a degree. Therefore, the preponderant effect expected is that due to ocean roughness, and it is only reasonable to accept it as the effect which is displayed in Figure 20. The wind speed dependence determined from the regression line of 0.155°K/knot is extremely, and probably somewhat fortuitously, close to the value of 0.16°K/knot determined prior to this analysis from other data as discussed earlier. The present result validates the earlier wind speed dependence which was used in ANTTEMP, at least at 1.4 GHz.

A final treatment of the data was performed in order to evaluate the absolute accuracy of S-194 as well as the stability and repeatability of the measurements from one EREP Pass to another and one mission to the next. A difference distribution of all the ocean data was computed by subtracting each calculated antenna temperature from the corresponding measured antenna temperature. The antenna temperature was calculated using ANTTEMP and the theoretical model for sea

temperature, salinity, wind speed, and atmospheric effects.
The plot of this difference distribution in °K versus Skylab
Pass Number is shown in Figure 21. Although each individual
pass may have a noticeable bias ranging from + 2.1°K for
Pass 38 to -1.9°K for Pass 40, the mean for all the data
analyzed is -0.0035°K with a standard deviation of 1.3°K. A
"t" test was run and the mean value of this distribution was
determined to be not significantly (t = -0.026) different
from zero. This indicates excellent agreement between the
model calculations and the average absolute level of the
measurements. However, there are apparent small systematic
changes in the absolute level of as much as 2°K from pass to
pass. The standard deviation of 1.3°K includes the effect
of this systematic change in level as well as errors in the
determination of the environmental parameters, instrumental
variations and noise and errors due to data quantization.
It indicates an absolute accuracy of about 1.3°K for the S-194
sensor.

CONCLUSIONS:

In conclusion the results of the analysis of the S-194
data demonstrate that it is indeed possible to make accurate
measurements of the earth's ocean areas from a satellite
with a passive microwave radiometer. Although S-194, at a
frequency of 1.4 GHz, is only relatively weakly dependent
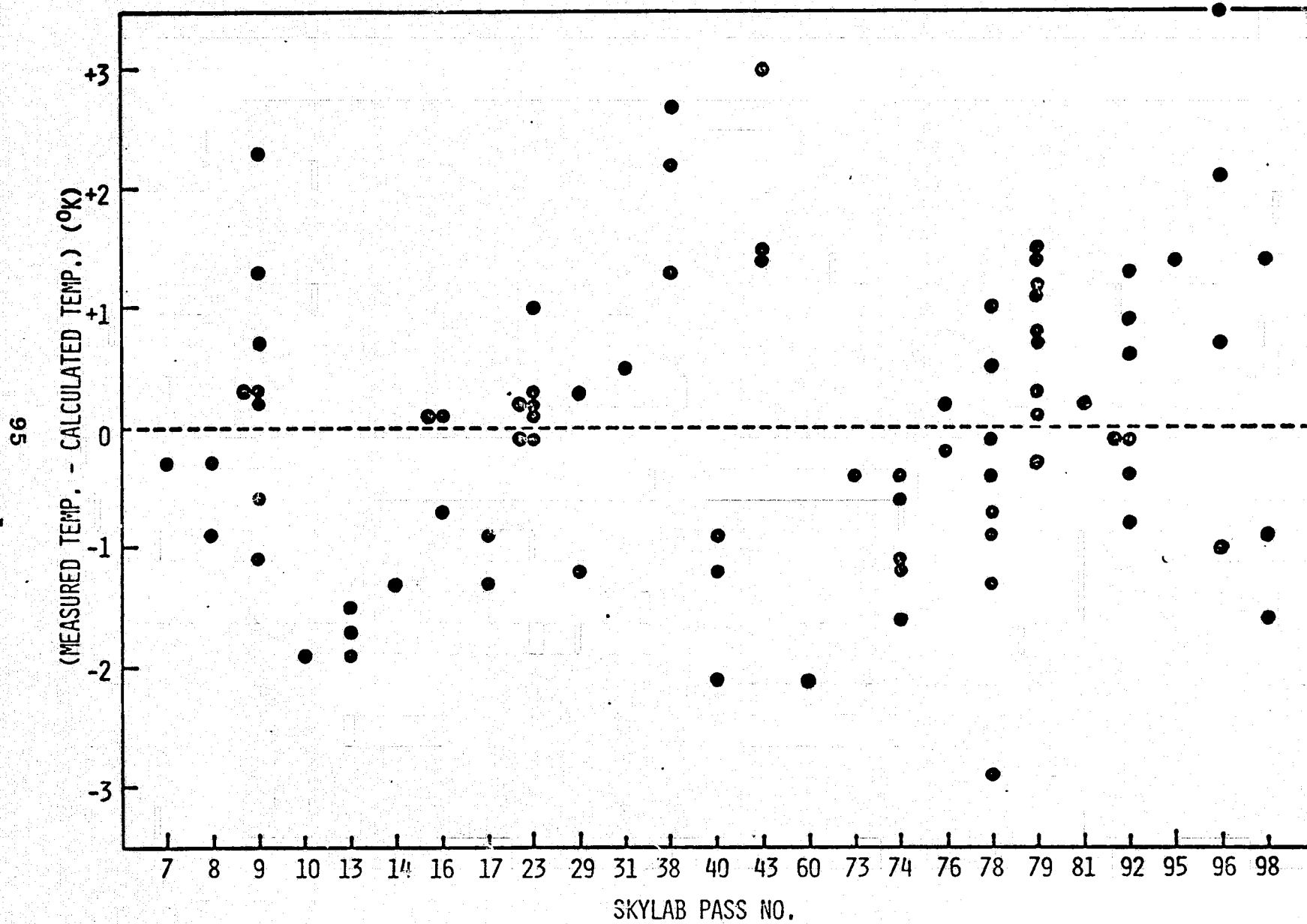upon marine environmental conditions, except for its dependence

94

Figure 21

upon salinity, compared to higher frequency radiometers, the rms absolute accuracy, of 1.3°K, of the measurements over a wide range in environmental conditions is quite good. Unfortunately, the footprint of S-194 is too large for a detailed study of land-water areas. However, we have shown that it is possible to accurately model complex regions such as lakes and bays and obtain excellent agreement between calculated and measured antenna temperatures. S-194 is very insensitive to ocean temperature, and it was not possible to obtain conclusive data regarding the measurement of the temperature of fresh water, for which it is more sensitive, because of the large footprint compared to fresh water areas. Therefore, S-194 is of very limited, if any, use in measuring surface water temperature. The large footprint of S-194 again limited the measurement of salinity in lakes or bay areas because of the large correction for the portion of the beam filled by land. The analysis of the ocean data shows that salinity measurements away from the influence of land can be made to an accuracy of about 2 PPT. A very clear but weak ocean roughness (wind speed) dependence was found of about 0.16°K/knot. This indicates that S-194 may be used to determine marine wind speeds to an accuracy of about ±8 knots. In order to measure either salinity or wind speed to these accuracies, ground truth on the other environmental parameters must be available. Under certain homogeneous conditions, it may be possible to measure relative changes

in salinity or wind speed to an even greater precision. Since S-194 is very insensitive to atmospheric water vapor, clouds and even rain, and is only weakly affected by molecular oxygen, the atmosphere serves principally to bias the measurements and S-194 is not useful as a meteorological instrument.

REFERENCES

1. Bracewell, R. N., Handbuch Der Physik, Vol. 54, 43-129, 1962.

2. Chandrasekhar, S., "Radiative Transfer," Dover Publ. Inc., New York, New York, 1960.

3. SKYLAB Program, Earth Resources Experiment Package, Sensor Performance Report, Vol. IV (S-193 R/S), #MSC-05528, NASA, October 30, 1974.

4. SKYLAB Program, Earth Resources Experiment Package, Sensor Performance Report, Vol. VI (S-194), #MSC-05528, NASA, September 6, 1974.

5. Saxton, J. A. and Lane, J. A., "Electrical Properties of Sea Water," Wireless Engineer, 269-275, October, 1952.

6. Ho, W. W., Love, A. W., and Van Melle, "Measurements of the Dielectric Properties of Sea Water at 1.43 GHz," NASA Contractor Report CR-2458, December, 1975.

7. Hollinger, J. P., "Microwave Properties of a Calm Sea," Branch Report No. 7110-2, AD#771374, August 15, 1973.

8. Hollinger, J. P., "Passive Microwave Measurements of Sea Surface Roughness," IEEE Trans. Geoscience Elect., Vol. GE-9, 165-169, July, 1971.

9. Swift, C. T., "Microwave Radiometer Measurements of the Cape Cod Canal," Radio Science, Vol. 9, No. 7, 641-653, July, 1974.

10. Stogryn, A., "The Apparent Temperature of the Sea at Microwave Frequencies," IEEE Trans. Antennas Propagation, Vol. AP-15, 278-286, March, 1967.

11. Meeks, M. L., and Lilley, A. E., "The Microwave Spectrum of Oxygen in the Earth's Atmosphere," Journal of Geophysical Research, 68, 1683-1703, 1963.

12. Van Vleck, J. H., "Absorption of Microwave by Oxygen," Physical Reviews, 71, 413-424, 1947.

13. Reber, E. E., "Absorption of the 4- to 6-Millimeter Wavelength Band in the Atmosphere," Journal of Geophysical Research, 77, 3831-3845, 1972.

14. Staelin, David H., "Measurements and Interpretation of the Microwave Spectrum of the Terrestrial Atmosphere near 1-Centimeter Wavelength," Journal of Geophysical Research, 71, 2875-2881, 1966.

15. Barrett, A. H., and Chung, V. K., "A Method for the Determination of High-Altitude Water-Vapor Abundance from Ground-Based Microwave Observations," Journal of Geophysical Research, 67, 4259-4266, 1962.

16. Van Vleck, J. H., "Absorption of Microwaves by Oxygen," Physical Reviews, 71, 413-424, 1947.

17. Paris, J. F., "Transfer of Thermal Microwaves in the Atmosphere," Thesis, Department of Meteorology, Texas A.&M, 1971

18. Thaddeus, P., "The Short-Wavelength Spectrum of the Microwave Background," Annual Review of Astronomy and Astrophysics, 10, 305-334, 1972.

19. Stogryn, A., "A Note on Brightness Temperature at Millimeter Wavelengths," IEEE Trans. Geosci. Electron., GS-13, 81-84, 1975.

20. Kraus, John D., "Radio Astronomy," McGraw-Hill Book Company, New York, New York, 1966.

21. Cox, C., and Munk, W., "Statistics of the Sea Surface Derived from Sun Glitter," J. Mar. Res., Vol. 13, 198-227, 1954

22. Cox, C., and Munk, W., "Measurements of the Roughness of the Sea Surface from Photographs of the Sun's Glitter," J. Opt. Soc. Amer., Vol. 44, 838-850, November, 1954.

23. "Oceanographic Atlas of the North Atlantic Ocean," U.S. Naval Oceanographic Office, Pub. No. 700, Washington, D.C., 1967.

24. Sverdrup, H. U., Johnson, M. W., and Fleming, R. H., "The Oceans," Prentice-Hall, Inc., Englewood Cliffs, New Jersey, 1970.

25. "Daily Weather Maps," Environmental Data Service, National Oceanographic and Atmospheric Administration, U.S. Department of Commerce, Washington, D.C.